Supporting Materials

Theoretical illumination of hydrogen-bonding networks and proton wire for the $CaMn_4O_5$ cluster of photosystem II. Elongation of Mn-Mn distances with hydrogen bonds.

M. Shoji[a*], H. Isobe[b], S. Yamanaka[c], Y. Umena[d], K. Kawakami[d], N. Kamiya[d], J.-R. Shen[b], K. Yamaguchi[e,f*],

[a] Center of Computational Sciences, Tsukuba University, Tsukuba, Ibaraki 305-8577, Japan
[b] Graduate School of Natural Science and Technology, Okayama University, Okayama 700-8530, Japan
[c] Graduate School of Science, Osaka University, Toyonaka, 560-0043
[e] Handairigaku Techno-Research, Toyonaka, Osaka 560-0043.
[d] The OUC Advanced Research Institute for Natural Science and Technology (OCARNA), Osaka City University, 3-3-138 Sugimoto, Sumiyoshi, Osaka 558-8585, Japan.
[f] NanoScience Design Center, Osaka University, Toyonaka, Osaka, 560-0043

SI Oxygen evolving complex of photosystem II

SI.1 An extended Kok cycle for water oxidation

Abundant Mn ion has been chosen in the native catalysts (OEC of PSII) for water oxidation. First-row transition metals such as Mn, Fe, Co have 3d electrons which often exhibit magnetism because of strong electron repulsions. Therefore multi-nuclear manganese oxide complexes are regarded as strongly correlated electron systems (SCES) as shown in refs. 36-44. Generally SCES are characterized by orbital, charge and spin degrees of freedom.[36] Particularly valence states of Mn ions are often variable with environmental effects, indicating the importance of charge degree of freedom in multi-nuclear manganese complexes such as the $CaMn_4O_5$ cluster of oxygen evolving complex (OEC) of photosystem II (PSII). Indeed two different valence configurations have been proposed for the dark stable resting state (S_1 state) of OEC of PSII. One of two paradigms is the low-oxidation-state model for the S_1 state consisted of four Mn(III) ions ; $Ca(II)Mn(III)_2Mn(III)_2O_5$. The other is the high-oxidation-state model with the mixed-valence (MV) configuration ; $Ca(II)Mn(III)_2 Mn(IV)_2O_5$. In this paper the latter model has been assumed to depict the Kok cycle for water oxidation as illustrated in the supporting Figure S1. On the other hand, Pace et al have assumed the low-oxidation-state model for the S_1 state as shown in refs. 52-55. They have presented a number of computational results that have been explained on the low-oxidation-state scenario. Therefore detailed discussions of the low-oxidation-state model are not repeated in this paper. On the other hand, present computational results have been explained on the basis of the high-oxidation-state model in conformity with the SP8 XRD result by Umena et al.[34,35] Careful examinations of the valence states of Mn ions are however crucial because internal reductions of Mn ions are often resulted in the model clusters without hydrogen bonding stabilizations as shown in the text.

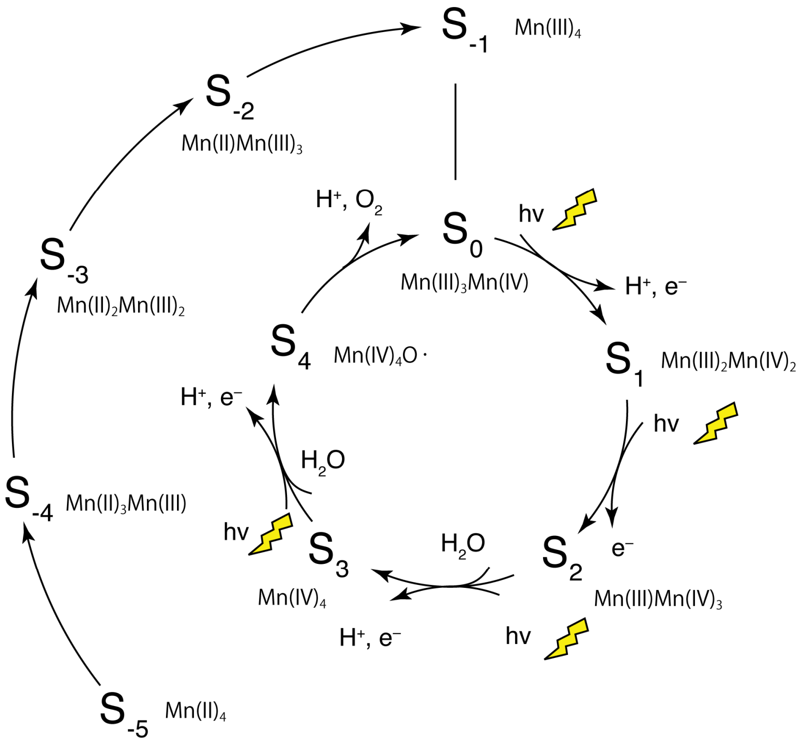

Figure S1. An extended Kok cycle for water oxidation of oxygen evolving complex (OEC) of photosystem II (PSII). The original Kok cycle for OEC of PSII is consisted of five steps (S_0-S_4). However, pre-S_0 steps (S_{-1} – S_{-5}) are discussed on the basis of the DFT computational results in relation to radiation damages of the $CaMn_4O_5$ cluster during the XRD experiment. The valence state of the Mn ions in the resting state (S_1) is taken to be $Mn(III)_2Mn(IV)_2$ in accord with the high-oxidation-state scenario of OEC of PSII. The valence states of other states obtained by reduction or oxidation of the $Mn(III)_2Mn(IV)_2$ structure are also given. The details of these states under theoretical debates are given in the text. The S_{-1} state of the high-oxidation-state model corresponds to the S_1 state in the low-oxidation-state model as discussed in the text.

SI.2 Working hypotheses (heuristic principles) revealed by the new XRD structure

The SP8 XRD structure of $CaMn_4O_5$ cluster (**1**) by Umena, Kawakami, Shen and Kamiya[34,35] have first elucidated positions of four coordinated water molecules to the active site, the $CaMn_4O_5$ cluster (**1**), and a number of other water molecules in OEC of PSII as shown in Fig. 1. Their structure has indeed revealed several important structural characteristics that enable quantum chemists to derive working hypotheses for consideration of possible mechanisms of water splitting reaction in eq. 1. One of such characteristics is the hydrogen-bonding networks around the $CaMn_4O_5$ cluster (**1**) in Fig. 1. For derivation of hypotheses concerning with the network, we consider the octet rule as a guiding principle to construct the tetrahedral structure for the oxygen dianion (O^{2-}) as shown in ref. 38. The types of coordination ligand fields and hydrogen bonding structures in **1** are classified into four groups as follows:[38]

A) oxygen dianion with three hydrogen bondings in Mn-oxo species,
B) oxygen dianion with two hydrogen bondings in binuclear Mn-O-Mn bond,
C) oxygen dianion with one hydrogen bond in trinuclear μ_3-$O(Mn)_3$ bond,
D) oxygen dianion without hydrogen bond in tetranuclear bond.

Fig. S2 illustrates notations of the oxygen dianions in **1** to explain the following hypotheses WH1-WH11 in ref. 38. In this paper WH4 was extended to include hydrogen bonding interactions in Figs. 4 -7.

(WH1) The oxygen site $O_{(4)}$ in Figs. S2, 1 and 3 is considered as type B oxygen dinanion because of the hydrogen bonds with $H_2O_{(11)}$ and that of NH_2 group of Arginine(R)357 amino acid residue. These hydrogen bondings indeed form the octet structure at $O_{(4)}$.

(WH2) The oxygen sites $O_{(1)}$, $O_{(2)}$ and $O_{(3)}$ in Figs. S2, 1 and 4 are considered as type C because of existence of three Mn-O bonds and one hydrogen bond: μ_3-$O_{(1)}$ with the hydrogen bond by $H_2O_{(10)}$, μ_3–$O_{(2)}$ with the hydrogen bond by NH_2 group of Arginine (R)357, and μ_3-$O_{(3)}$ with the hydrogen bond by NH group of Histidine (His) 337. All these O sites satisfy the octet rule.

(WH3) The oxygen site $O_{(5)}$ is considered as type D in Figs. S2 and 1 because three Mn-$O_{(5)}$ bonds and one Ca(II)-$O_{(5)}$ bond are formed with this oxygen dianion, forming the octet structure.

(WH4) The proton release pathway (PRP I) via hydrogen bonding network : $H_2O_{(1)}$ – Asparitic acid (Asp) 61- $H_2O_{(8)}$ – $H_2O_{(9)}$ -$H_2O_{(2)}$, where $H_2O_{(1)}$ (and $H_2O_{(2)}$) directly coordinated to $Mn_{4(a)}$ is assumed to have strong acidity to afford two electrophilic H-bonds. Similarly, $H_2O_{(8)}$ coordinated to actoxy (R-CO_2) anion

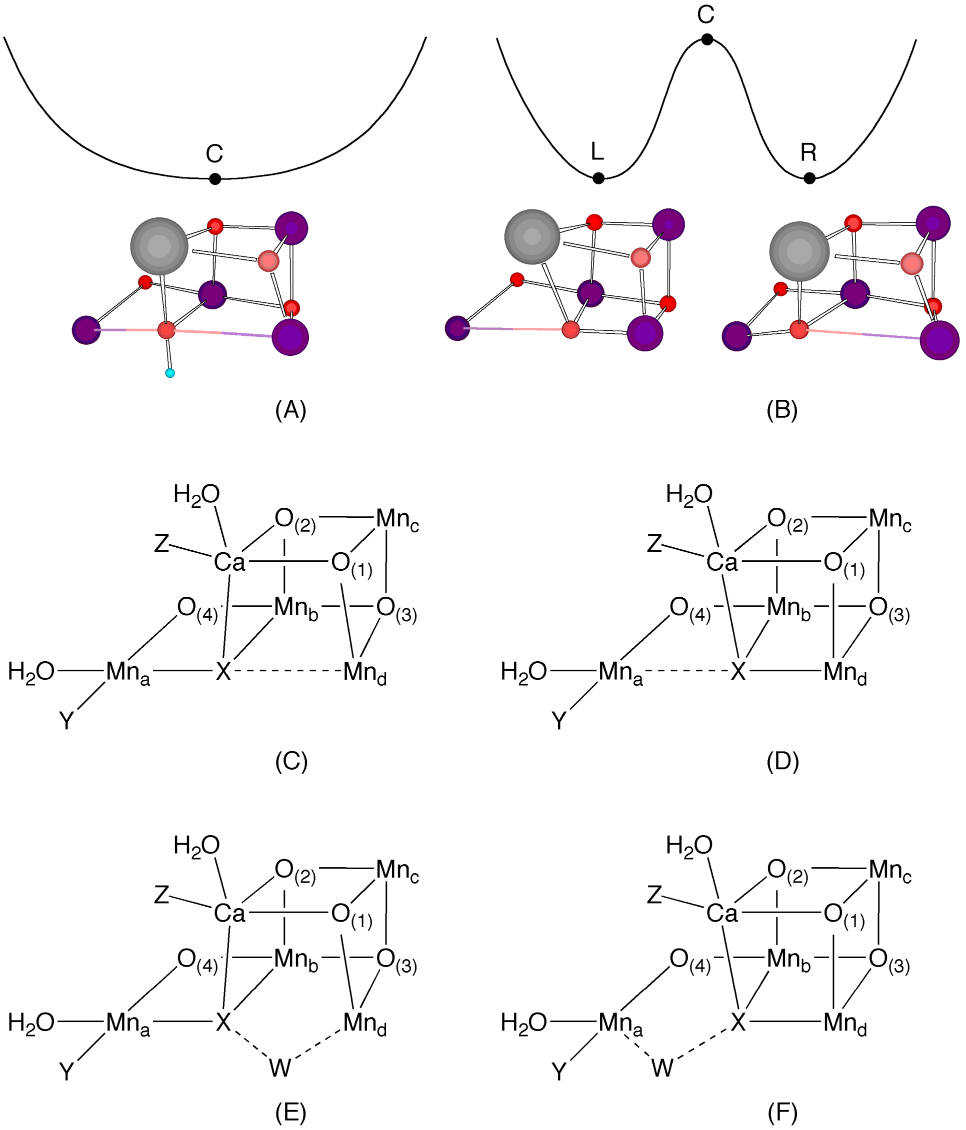

(A) (B)

(C) (D)

(E) (F)

Figure S2 The notations of bridge oxygen dianions are given in accord with the SP8 XRD structure (ref. 34): $Mn_{4(a)}$, $Mn_{3(b)}$, $Mn_{2(c)}$ and $Mn_{1(d)}$. The octet rule around the oxygen dianion has been assumed as a guiding principle for analysis of hydrogen bonding interactions in OEC of PSII. The working hypotheses (WH1-WH11) have been proposed on the basis of the hydrogen bonding networks in Figs. 2-7 in the text. The broken-symmetry left (L)- and right (R)-elongated structures of the $CaMn_4O_5$ clusters are obtained by the full geometry optimizations by the use of UB3LYP.

group of Asp61 is considered to exhibit the same ability. This network is coupled with the Lysine (Lys)317 and chloride anion that are connected with the proton release pathway as shown in Figs. S2, 1 and 2.

(WH5) The proton release pathway (PRP II) via hydrogen bonding network : $H_2O_{(3)}$ – - $H_2O_{(5)}$ – $H_2O_{(7)}$ (and $H_2O_{(3)}$ – $H_2O_{(5)}$ – $H_2O_{(6)}$ – $H_2O_{(7)}$) –Tyrosine - (Y)161(Phe-OH) – His190 –Asparagine(Asn) 298 , where $H_2O_{(3)}$ is directly - coordinated to Ca(II), providing two electrophilic H-bonds as shown in Fig. 1.

(WH6) The other $H_2O_{(4)}$ coordinated to Ca(II) forms the hydrogen bonding with Phe-OH group of Y161 and C=O group of Glutamine(Gln)165. The hydrogen-bonding network fixes the phenoxy radical Y_Z formed in the electron transfer process as shown in Figs. 1 and 4.

(WH7) The electron transfer (ET) occurs through the proton-coupled electron-transfer (PCET) pathway between Y161 and His190 in combination with through-bond interaction via π net work: Y161- His190- Phe186 – Ile290 – C=O of E ring of P680.

(WH8) The electron transfer (ET) is feasible through the hydrogen-bonding network: $CaMn_4O_5$ ($Mn_{1(a)}$) – Glu189- $H_2O_{(7)}$ –Y161.

(WH9) $H_2O_{(5)}$ and $H_2O_{(9)}$ connecting with water channel form the H-bonding with $H_2O_{(3)}$ coordinated to Ca(II) and $H_2O_{(2)}$ coordinated to $Mn_{a(4)}$, respectively. This in turn means that $H_2O_{(2)}$ and $H_2O_{(3)}$ are converted into molecular oxygen in water splitting reaction at OEC of PSII in eq. (1).

(WH10) Formal high-valent Mn(V)=O species (its derivatives •Mn(IV)=O• and ••Mn(III)=O) is an active intermediate for water splitting reaction at OEC of PSII.

(WH11) High-valent Mn(IV)=OH species is an active intermediate for the O-O bond formation of water splitting reaction at OEC of PSII.

Present QM and QM/MM computations have been performed to examine these working hypotheses (WH) in ref. 38 (WH4 in particular) revealed on the basis of the SP8 XRD structure.[34,3] Concerning with WH9, the bridge oxygen $O_{(5)}$ site is also a candidate of reaction site for the O-O bond formation as discussed in refs, 37, 39 and 42 because the bridge oxygen $O_{(4)}$ site play a role to suppress degradation of the cluster structure. Scope and applicability of WH1-11 have been examined in our UB3LYP computations in these papers.

SII Broken-symmetry approaches to strongly correlated electron systems

SII.1 Universal MO-VB approach via BS hybrid DFT calculations

(A) Necessity of BS method for Mn complexes

In the supporting material theoretical backgrounds of this paper are briefly summarized for lucid understanding of the computational results of the $CaMn_4O_5$ clusters (**1**) of OEC of PSII, particularly in relation to the internal and semi-internal reductions of Mn(IV) ions revealed by UB3LYP computational procedures. The four-electron oxidation process of water in eq. 1 is often catalyzed by artificial binuclear manganese complexes[69]. Therefore the water oxidation is regarded as a four-electron oxidation process from the Mn(III)-Mn(III) pair to the Mn(V)-Mn(V) pair in the sense of organometallic chemistry where electron pair transfer is a basic concept.[68] However, the photo-induced electron-transfer in eq. 1 is a one-electron process, and therefore four photons are necessary for four electron oxidation of a water molecule. This implies that the open-shell mixed-valence (MV) configurations, Mn(III)-Mn(IV) and Mn(IV)-Mn(V), play important roles for one-electron transfer processes coupled with one-electron photoexcitation, namely one-electron oxidation of the manganese ions, though these configurations are transient states that are hardly detected experimentally. The magnetic measurements[71] have elucidated that the active Mn(III)-Mn(III) complex is not a closed-shell species with stable electron pair bonds but an open-shell antiferromagnetic (AF) species with the localized electrons with local spins responsible for one-electron transfer. [72]

Electron-electron repulsion effects play important roles for electron localizations in antiferromagnetic (AF) transition-metal compounds such as multi-nuclear Mn complexes that are candidates for artificial catalysts for water oxidation.[71] Therefore these transition metal complexes are often referred to as strong correlation electron systems (SCES) in material science. Here general independent particle model involving the non-conventional broken-symmetry (BS) method, for example noncollinear spin-flustrated configuration, has been used as first step toward SCES that exhibit flexible geometrical, labile electronic and spin structures arising from the breaking of orbital, charge and spin degrees of freedom as shown in refs. 36-43. For example, a formal double bond system Mn=O=Mn is not a closed-shell in the sense of organometallic chemistry[68] but an open-shell species •Mn-O-Mn• with local spins that exhibit the AF behavior, namely the temperature-dependent paramagnetism.[72] This in turn means that these labile manganese oxides are unstable, indicating their stabilization by confinement materials such as protein, polyoxometallate (POM). On the basis of these theoretical backgrounds, we have proposed a theoretical picture that metalloenzymes are regarded as confined states of SCES with proteins, where hydrogen bonding act effectively for regulation of biological functions, and photo-induced one-electron transfers are also feasible.[68,72-74] Metal-organic framework (MOF), polyoxometallate (POM) and nanotube are used for confinement materials of SCES in the artificial water oxidation systems. [43,73]

The molecular orbital (MO) approaches such as extended Huckel method provide conventional orbital pictures for organometallic compounds with stable electron pair bonds that are often regarded as non-magnetic weak correlation systems.[68] On the other hand, the atomic orbital (AO) approaches such as the VB model are rather useful for qualitative understanding of inorganic magnetic compounds with localized spins, namely SCES. The MO- and AO-limits lead to a simple question; How about many intermediate cases between MO and AO limits? As shown previously,[S1,S2]the broken-symmetry (BS) MO methods can describe continuous variations of the nature of chemical bonds from the MO (weak correlation) limit to the VB (strong correlation) limit, depending on the strength of the HOMO-LUMO mixing that is dependent on the electron-electron repulsion (U parameter in the Hubbard model and LDA+U model in DFT). Thus the BS approach is one of the universal MO-VB theoretical model that is applicable to various intermediates cases.

Nowadays strongly correlated electron systems (SCES) such as manganese-oxide clusters[S3,S4] are investigated by broken-symmetry (BS) methods that include spin-polarized (unrestricted; U) Hartree-Fock (UHF) [S5)], Hartree-Fock-Slater (UHFS) [S6)], DFT (UDFT)[54] and hybrid UHF-UDFT[57] approximations. These broken symmetry (BS) computational methods provide broken-symmetry (spontaneously localized via strong electron repulsion) molecular orbitals (MO) concepts that are useful and handy for lucid understanding of chemical bonds of the transition metal complexes such as the $CaMn_4O_5$ clusters of OEC of PSII. For example, one-electron oxidation of manganese ions is easily understood based on the localized electron (spin) on the atoms as discussed in ref. 41. Here basic concepts of the BS method are briefly explained as shown below I relation internal reductions of high-valent Mn ions of OEC of PSII. The scope and applicability of the BS methods have been examined on the basis of the multi-reference (MR) coupled-cluster (CC) methods in the case of small systems.

(B) Theoretical backgrounds of the BS method

As shown in refs. S5, S6 and ref. 37, the BS MOs are obtained by the HOMO-LUMO mixing procedure[S3] in the self-consistent-field (SCF) approach.[S2] However, BS MO orbitals for strongly correlated electrons obtained by the

HOMO-LUMO mixing are often complex because of spin polarization effects of other labile electrons. In order to elucidate mutual relationships between BS MO and simple traditional MO pictures, the first-order density matrix ($\rho_1(\mathbf{r}_1,\mathbf{r}_2)$) of the UHF, UHFS, UDFT, UHF-UDFT and other related BS solutions is diagonalized as [S1,S2)]

$$\rho_1(\mathbf{r}_1,\mathbf{r}_2) = \sum_i \int \psi_i^\dagger \psi_i \, \mathrm{ds} = \sum_i n_i \phi_i^\dagger \phi_i \,, \qquad \text{(s1)}$$

where ψ_i denotes the BS MO *i*, and ϕ_i and n_i mean, respectively, the symmetry-adapted (SA) molecular orbitals (MO) and the occupation number. The BS MOs are expressed with mixing of the bonding and antibonding MOs pair as[S3,S4)]

$$\psi_i^+ = \cos\theta_i \phi_{HOMO-i} + \sin\theta_i \phi_{LUMO+i}^* \qquad \text{(s2a)}$$
$$\psi_i^- = \cos\theta_i \phi_{HOMO-i} - \sin\theta_i \phi_{LUMO+i}^* \qquad \text{(s2b)}$$

where θ_i denotes the orbital mixing parameter determined by the self-consistent-field (SCF) calculations. The number i is usually larger than 1 because of many spin polarized bonds as shown in refs. 36-43. HOMO and LUMO denote, respectively, the highest-occupied and lowest-unoccupied molecular orbitals, respectively. Since ϕ_{HOMO-i} and ϕ_{LUMO+i}^* are symmetry-adapted (SA) delocalized orbitals and usually belong to different spatial symmetries, BS MOs are often spatially symmetry-broken; namely they are more or less localized orbitals, showing a characteristic feature of the broken-symmetry (BS) methods. As shown in refs. 37 and 39, the number (i) of the BS MOs in equation (s2) is over ten in the case of the $CaMn_4O_5$ clusters (**1**), indicating that complete active spece (CAS) for symmetry-adapted (SA) CI-type treatments[7] of **1** are larger than twenty-orbitals twenty electrons {20, 20}. SA CAS self-consistent-field (SCF) {20,20} and CASSCF PT2(second-order perturbation) are hardly applicable to the active sites (**1**) of OEC[1,2)], even now. On the other hand, such large CAS CI approach becomes feasible by the density matrix renormalyzed group (DMRG) technique.[44]

The orbital overlap T_i between the up- and down-spin BS MOs in equation s2) is introduced to express localizability of broken-symmetry (BS) orbitals obtained by the HOMO-LUMO mixing, namely continuous MO-AO transition.[S5)] It is defined as

$$T_i = \left\langle \psi_i^+ \middle| \psi_i^- \right\rangle = \cos 2\theta. \qquad \text{(s3)}$$

The occupation numbers of the natural molecular orbitals (MO) are expressed by the orbital overlap as follows: [S4,S6]

$$n_{HOMO-i} = 1 + T_i \qquad \text{(s4a)}$$
$$n_{LUMO+i} = 1 - T_i \qquad \text{(s4b)}$$

The orbital overlap T_i becomes 1.0 in the case of the closed-shell case; $\psi_i^+ = \psi_i^- = \phi_i$;

this means that BS MOs reduce to the conventional closed-shell MOs at the instability threshold (MO limit), showing that BS MOs are natural generalization of the MO approach to non-closed-shell species such as $CaMn_4O_5(H_2O)_4$ (**1a**). The closed-shell MO pictures by spin-restricted (R) DFT (RDFT) methods in combination with cluster symmetry are already used for beautiful explanation of stable organometallic cluster compounds.[68] On the other hand, T_i is 0.0 for the complete mixing case ($\theta_i = \pi/4$); this corresponds to the pure open-shell state (AO limit): for example, localized d-electrons in **1**. Furthermore, the BS MOs with smaller nonzero T_i values describe labile d-p chemical bonds with moderate diradical character[62,63,71] in **1**. These bonds play crucial roles for water splitting reaction at OEC of PSII.

In order to express the decrease of chemical bonding via orbital symmetry breaking, the effective bond order b_i is defined by[S2]

$$b_i = \frac{n_{HOMO-i} - n_{LUMO+i}}{2} = \frac{(1+\cos 2\theta_i) - (1-\cos 2\theta_i)}{2} \qquad \text{(s5a)}$$

$$= \cos 2\theta_i = T_i, \qquad \text{(s5b)}$$

where n_{HOMO-i} and n_{LUMO+i} denote the occupation numbers of the bonding (HOMO-i) and antibonding (LUMO+i) natural MOs (NMOs), respectively. The effective bond order (b_i) is nothing but the orbital overlap between BS MOs under the generalized MO (GMO) approximation in eq. (s2). Here hybrid DFT Kohn-Sham orbitals[56,57] are also regarded as generalized MO after the natural orbital analysis in eq. s1.

The valence-bond (VB) concepts are also introduced for theoretical understanding of chemical bonds in strongly correlated electron systems (SCES) such as open-shell transition-metal complexes **1**. In order to extract the VB concepts under the BS DFT approximation, the localized MO (LMO) are defined as the completely spin polarized BS MOs as[S1,S2,S8,S9]

$$\psi_i^+(\theta_i = \pi/4) = \frac{1}{\sqrt{2}}\left(\phi_{HOMO-i} + \phi^*_{LUMO+i}\right) = \phi_{\mathrm{LMOa}} \qquad \text{(s6a)}$$

$$\psi_i^-(\theta_i = \pi/4) = \frac{1}{\sqrt{2}}\left(\phi_{HOMO-i} - \phi^*_{LUMO+i}\right) = \phi_{\mathrm{LMOb}}, \qquad \text{(s6b)}$$

where LMOa and LMOb are mainly localized on the a and b sites of manganese ions of **1**, respectively, but they have very small tails because of their orthogonality. The LMOs are responsible for derivation of Heisenberg localized spin Hamiltonian model[76] that is utilized for analysis of ENDOR results for **1.** [24-31] In fact, several HOMO-LUMO pairs for d-electrons in **1** have almost zero overlaps, indicating the localized nature of d-electrons as shown in refs. 36-43. However, it is noteworthy that LMOs are quite different from the atomic orbitals (AO) in the simple VB theory because LMO are orthogonal and still molecular orbitals in nature. Then the expression of LMOs by AO-like orbitals in the BS approach is regarded as just symbolic for qualitative and lucid understanding of electronic and spin structures of **1**.

In order to extract the VB configuration interaction (CI) concepts from the BS DFT calculations, the delocalized MO expression via natural MO(NMO) can be transformed into LMO expression. To this end, the BS MOs in equation (s2) are re-expressed with LMOs in Equation (s6) as follows[S1,S2,S8,S9]

$$\psi_i^+ = \cos\omega_i\phi_{\mathrm{LMOa}} + \sin\omega_i\phi_{\mathrm{LMOb}} \tag{s7a}$$

$$\psi_i^- = \cos\omega_i\phi_{\mathrm{LMOb}} + \sin\omega_i\phi_{\mathrm{LMOa}}, \tag{s7b}$$

where the mixing parameter ω_i is given by $\theta_i + \pi/4$. The BS MO configuration can be expanded with using LMOs to the VB CI form as

$$\begin{aligned}\Psi_{\mathrm{BSI}} &= \left|\psi_i^+ \overline{\psi_i^-}\right| \\ &= \left|\left(\cos\omega\phi_{\mathrm{LMOa}} + \sin\omega\phi_{\mathrm{LMOb}}\right)\overline{\left(\cos\omega\phi_{\mathrm{LMOb}} + \sin\omega\phi_{\mathrm{LMOa}}\right)}\right|\end{aligned} \tag{s8a}$$

$$= \frac{1}{2}\left\{\sqrt{2}\cos 2\omega\Phi_{\mathrm{SD}} + \sqrt{2}\Phi_{\mathrm{TD}} + \sin 2\omega\left(\Phi_{\mathrm{ZWa}} + \Phi_{\mathrm{ZWb}}\right)\right\}, \tag{s8b}$$

where the pure singlet (SD) and triplet (TD) covalent (CV) wavefunctions are given by

$$\Phi_{\mathrm{SD}} = \frac{1}{\sqrt{2}}\left\{\left|\phi_{\mathrm{LMOa}}\overline{\phi_{\mathrm{LMOb}}}\right| + \left|\phi_{\mathrm{LMOb}}\overline{\phi_{\mathrm{LMOa}}}\right|\right\} \tag{s9a}$$

$$\Phi_{\mathrm{TD}} = \frac{1}{\sqrt{2}}\left\{\left|\phi_{\mathrm{LMOa}}\overline{\phi_{\mathrm{LMOb}}}\right| - \left|\phi_{\mathrm{LMOb}}\overline{\phi_{\mathrm{LMOa}}}\right|\right\}. \tag{s9b}$$

On the other hand, zwitterionic (ZW) configurations are resulted from the charge transfer from ϕ_{LMOa} to ϕ_{LMOb} (vice versa) as follows:

$$\Phi_{\mathrm{ZWa}} = \left|\phi_{\mathrm{LMOa}}\overline{\phi_{\mathrm{LMOa}}}\right|, \quad \Phi_{\mathrm{ZWb}} = \left|\phi_{\mathrm{LMOb}}\overline{\phi_{\mathrm{LMOb}}}\right|. \tag{s10}$$

The low-spin (LS) BSI MO configuration involves both singlet diradical (DR) and ZW configuration as in the case of the VB CI, but it also includes the pure triplet DR (TD) component, showing the spin-symmetry breaking property in the BS solution. Similarly, the low-spin (LS) BSII MO configuration is expressed by

$$\begin{aligned}\Psi_{\mathrm{BSII}} &= \left|\psi_i^- \overline{\psi_i^+}\right| \\ &= \frac{1}{2}\left\{\sqrt{2}\cos 2\omega\Phi_{\mathrm{SD}} - \sqrt{2}\Phi_{\mathrm{TD}} + \sin 2\omega\left(\Phi_{\mathrm{ZWa}} + \Phi_{\mathrm{ZWb}}\right)\right\}.\end{aligned} \tag{s8c}$$

The LS BSII MO solution also involves the singlet DR and ZW configurations, together with the pure triplet component.[S9,S10] Thus the spin symmetry breaking is inevitable for open-shell species in the case of the single-determinant (reference) BS solution; the unrestricted Hartree-Fock (UHF) and Kohn-Sham DFT (UDFT) models belong to this category. Nevertheless, BS methods can be regarded as a convenient and handy procedure to elucidate characteristic but continuous transitions from delocalized to localized MOs for open-shell transition-metal clusters such as **1**. Both orbital and spin symmetries should be conserved in finite quantum systems in contrast with infinite systems where the recovery of symmetry is impossible because of real phase transitions.[S1,S2,S10] Then the recovery of symmetry is performed for quantitative discussions of finite clusters such as $CaMn_4O_5(H_2O)_4$ (**1a**) as shown in refs. 36-43.

SII.2 Recovery of symmetry breaking via quantum resonance

The BS method based on a single Slater determinant is only a first step toward SCES such as Mn oxide species for which many Slater determinants are necessary for more exact descriptions. One of the multi-determinant approaches is the resonating BS （RBS） method that uses the superposition of BS solutions obtained in section SII.1(B). For example, the BSI and BSII solutions are degenerate in energy. Then the resonance of them is feasible if the quantum-mechanical interaction term between them is not negligible: [S10]

$$\Phi_{\mathrm{RBS(+)}} = \frac{1}{\sqrt{2}}\left(\Phi_{\mathrm{BSI}} + \Phi_{\mathrm{BSII}}\right) \tag{s11a}$$

$$= \frac{1}{\sqrt{2}}\left\{\sqrt{2}\cos 2\omega \Phi_{\mathrm{SD}} + \sin 2\omega\left(\Phi_{\mathrm{ZWa}} + \Phi_{\mathrm{ZWb}}\right)\right\}, \tag{s11b}$$

$$\Phi_{\mathrm{RBS(-)}} = \frac{1}{\sqrt{2}}\left(\Phi_{\mathrm{BSI}} - \Phi_{\mathrm{BSII}}\right) \tag{s12a}$$

$$= \Phi_{\mathrm{TD}}. \tag{s12b}$$

The in- and out-of-phase resonating BS (RBS) solutions are nothing but the pure singlet and triplet states wave functions, respectively. Thus the spin symmetry is recovered since the interaction matrix element between BS configurations is not zero for finite systems. The chemical bonding between a and b sites is expressed with the mixing of the singlet diradical (SD) and ZW configurations under the LMO approximation. The valence-bond (VB) CI type explanation of electronic structures becomes feasible under the LMO CI approximation. For example, the effective bond order becomes zero for the pure SD state, but it increases with the increase of mixing with the ZW configuration until the ZW/SD ratio becomes 1.0, namely closed-shell limit. Thus the BS CI computational results can be utilized to extract the VB CI pictures based on the LMO CI methods.[S2] The so-called Penny's (second-order) bond order related to the Heisenberg model is also utilized in the LMO (VB) approximation (see ref. S2).

On the other hand, the molecular orbital concepts are also generalized on the basis of the natural orbital analysis of broken-symmetry (BS) solutions. The Coulson's (first-order) bond order is well-accepted in the MO method. In order to obtain the Coulson's effective bond order for the RBS(+) solution, it is transformed into the symmetry-adapted NMO expression as

$$\Psi_{\mathrm{RBS}(+)} = \frac{1}{\sqrt{2(1+T_i^2)}}\Big\{\big(1+\cos 2\theta_i\big)\big(\phi_{HOMO-i}\overline{\phi_{HOMO-i}}\big(- \big(1-\cos 2\theta_i\big)\big(\phi^*_{LUMO+i}\overline{\phi^*_{LUMO+i}}\big(\Big\} \quad \text{(s13)}$$

where the first and second terms denote the ground and doubly excited configurations, respectively. This MO-CI picture is useful for theoretical understanding of labile chemical bonds with moderate orbital overlaps in equation (s3). For example, manganese oxo (Mn=O) and μ-oxo (Mn-O-Mn) bonds[71] in high-valent manganese oxides such as **1** exhibit such behaviors: this is an origin of chameleonic (oxyl radical/electrophilic) reactivity of these bonds as shown in ref. 38. The effective bond order (B) for $\Phi_{\mathrm{RBS}(+)}$ is introduced to express the nature of these labile chemical bonds as

$$B_i = \frac{n_{HOMO-i}\big(RBS(+)\big) - n_{LUMO+i}\big(RBS(+)\big)}{2} \quad \text{(s14a)}$$

$$= \frac{\big(1+T_i\big)^2 - \big(1-T_i\big)^2}{2\big(1+T_i^2\big)} = \frac{2T_i}{1+T_i^2} \quad \text{(s14b)}$$

$$= \frac{2b_i}{1+b_i^2} \geq b_i\,. \quad \text{(s14c)}$$

The effective bond order (B_i) after elimination of triplet contamination part is larger than that (b_i) of the BS solution itself. This is not at all trivial, indicating that BS computational results without symmetry recovery are often biased to oxyl-radical picture arising from high-spin component: the BS method may overestimate the inner reduction arising from this character. The diradical character (y_i) after spin contamination is defined by the weight of the doubly excited configuration under the NMO approximation as

$$y_i = 2W_{\mathrm{D}} = \frac{\big(1-T_i\big)^2}{1+T_i^2} = 1 - \frac{2T_i}{1+T_i^2} \quad \text{(s15a)}$$

$$= 1 - B_i \quad \text{(s15b)}$$

The diradical character y is directly related to the decrease of the effective bond order B:

these indices are used for diagnosis of radical reactivity of manganese oxide species such as **1**.

In the multi-nuclear transition-metal complexes such as **1**, the spin polarized orbital pairs are over ten (i>10)[39-44], indicating the necessity of total chemical indices such as polyradical character (*Y*), total effective bond orders (*b and B*).

$$b=\sum_i b_i,\quad B=\sum_i B_i\ ,\quad Y=\sum_i y_i \tag{s15c}$$

Several broken-symmetry (BS) solutions are nearly (or completely) degenerate in energy in manganese oxide clusters, indicating the necessity of configuration mixing (CI) of them to obtain the true ground and lower-excited states as follows.[S2,S10]

$$\Phi_{\mathrm{BS\ CI}}=\sum_i C_{ij}\Phi_{BSj} \tag{s16}$$

where C_{ij} denotes the CI coefficient. The simple pairing relation in Equations s2 and s8 often is removed out under BS CI as in the case of CASSCF, MSSCF and DMRG. Information entropy (I) is introduced as an alternative to the effective bond orders for labile chemical bonds by using the occupation numbers (*n*) of the natural orbitals of BS CI, CASSCF, MSSCF and DMRG that are obtained by eq. s1.[S2,S10]

$$I_i=-n_i\ln n_i. \tag{s17a}$$

Therefore information entropy for closed-shell pair is given by

$$I_c=-2\ln 2. \tag{s17b}$$

The normalized information entropy is defined as an alternative to the effective bond order by

$$I_n=\frac{n_i\ln n_i}{2\ln 2}. \tag{s17c}$$

The above index can be used for open-shell systems in general.

SII.3 Pair and spin correlation functions and chemical indices for SCES

The spin densities appear under the BS approximation even in the antiferromagnetic (AF) low-spin (LS) singlet-type BS configuration, though they should disappear in the exact singlet state. In this paper we have utilized the spin densities to depict a spin vector models such as (↑↓↓↑), leading to a basic question regarding what is the spin density in the LS BS solution used for discussions in this paper; only spin contamination errors? Therefore physical basis of appearance of the spin density should be clarified in the case of antiferromagnetic (AF) low-spin (LS) BS solutions. Indeed, important roles of spin densities emerge via the analysis of pair and spin correlation functions of the BS solutions as shown in our early papers.[S2,S9] The on-site pair function (P_2) for electrons with different spins is given by

$$P_2(\mathbf{r}_1,\mathbf{r}_1;\mathbf{r}_1,\mathbf{r}_1)=\left[P_1(\mathbf{r}_1,\mathbf{r}_1)^2-Q(\mathbf{r}_1,\mathbf{r}_1)^2\right]\Big/2, \qquad \text{(s18)}$$

where $P_1(\mathbf{r}_1,\mathbf{r}_1)^2$ and $Q_1(\mathbf{r}_1,\mathbf{r}_1)^2$ denotes, respectively, the density and spin density. This means that the magnitude of spin density is parallel to the size of Coulombic hole for electrons with different spins in strongly correlated electron systems (SCES). Then the unpaired electron density *U(r)* (not U in the HHH model) responsible for deviation from the single determinant is expressed by the square of spin density under the BS approximation [S2] as

$$\begin{aligned} U(\mathbf{r}_1) &= \Sigma\ n_i(2-n_i) \\ &= \Sigma\ (1-T_i^2)=Q(\mathbf{r}_1,\mathbf{r}_1)^2=Q(\mathbf{r}_1)^2. \end{aligned} \qquad \text{(s19a)}$$

where n_i denotes the occupation number of the natural orbital (NO) i. The magnitude of spin densities reported in various recent BS calculations can be understood from the view point of nondynamical correlations between electrons with different spins[S1,S2]; namely strong electron repulsion effects. Therefore the unpaired spin density can be used a diradical character based on the occupation number of NO as shown in s19a. The U(r)-value becomes indeed a useful index of radical character for the post BS methods because the occupation numbers are easily obtained by CASCI, CASSCF, etc. The spin density index is introduced to express the characteristic behavior of the spin density in the BS approach as

$$Q_i(\mathbf{r}_1,\mathbf{r}_1)=\sqrt{U_i(r)}=\sqrt{1-T_i^2},Q(\mathbf{r}_1,\mathbf{r}_1)=\sum_i Q_i(\mathbf{r}_1,\mathbf{r}_1) \qquad \text{(s19b)}$$

The sign of spin densities is a basic problem under the BS approximation. In order to elucidate this problem, the spin correlation function is introduced since it can be observed in the case of infinite systems by the neutron diffraction technique. The spin correlation function $K_2(\mathbf{r}_1,\mathbf{r}_2)$ is approximately given by

$$K_2(\mathbf{r}_1,\mathbf{r}_2)=\int \mathbf{s}(1)\cdot\mathbf{s}(2)P_2(\mathbf{r}_1,\mathbf{r}_2;\mathbf{r}_1,\mathbf{r}_2)\mathrm{ds} \qquad \text{(s20a)}$$

$$\approx Q(\mathbf{r}_1)Q(\mathbf{r}_2). \qquad \text{(s20b)}$$

where P_2 denotes the second-order density matrix. The $K_2(\mathbf{r}_1,\mathbf{r}_2)$ function is indeed determined by the neutron-diffraction procedure for magnetic materials with long-range order. However such technique cannot be applicable for small magnetic clusters with short-range order because of fast spin exchange. Nevertheless the spin correlation function has a physical meaning even for finite systems. It means that the spin correlation is singlet-type if the sign of spin density product is negative; (↑↓) or (↓↑) (see also equation s22 below). In this paper, we have used such a pictorial expression, for example (↑↓↓↑), of the antiferromagetic (AF) low-spin (LS) singlet state. The sign of spin density is closely related to the spin correlation function under the BS approximation.

Although the spin densities arising from the first-order density $P_1(\mathbf{r}_1,\mathbf{r}_2)$ disappears at the pure singlet state, the unpaired electron density (U) and spin correlation function (K_2) still exist as important spin and electron correlation indices even in the resonating BS (RBS) and symmetry-adapted MR wave functions such as CASSCF, CASDFT, CAS coupled-cluster (CC) and DMRG by the use of BS NO[S2,S10]. Therefore sign and magnitude of spin densities for **1** in Tables S1-S3 in this article should be understood from the above theoretical viewpoints. The pair and spin correlation functions can be used to elucidate the nature of chemical bonds in the case of RBS and MR approaches as alternative indices for spin density at the BS UB3LYP level of theory. Instead of MR wavefunction approaches, the exact diagonalization of spin Hamiltonian models involving effective exchange integrals (Jab) obtained by BS calculations has been performed to elucidate low energy levels for strongly correlated electron systems (SCES) in our spin-projected approach.[72]

Thus several chemical indices are introduced before and after spin projections of BS solutions and BS CI.[S11] They have been applied to elucidate the nature of chemical bonds in metalloenzymes such as **1**. These indices are useful for theoretical explanation of labile chemical bonds in the species. The chemical indices, n_{LUMO}, b_i, B_i, I_i, Q_i and y_i, are mutually related in the generalized MO (GMO) approach based on BS calculations. Functional behaviors of these chemical indices on the orbital overlap (T_i) are illustrated in Figure S3. The spin density index Q_i increases sharply with the decrease of the orbital overlap as shown in Fig. S3 in sharp contrast to the diradical character (y_i) that is directly related to the effective bond order (B_i) after spin projection as shown in equation (s15b). As shown in refs. 36,38 and 43, non-negligible spin densities indeed appear even on the oxygen dianions of **1** if the Mn-Mn and Mn-O bond distances revealed by the SP8 XRD[34,35] are assumed for DFT calculations. This implies that the SP8 XRD distances are a little overestimated within the error range of the XRD experiment, supporting the computational results in Tables 1 and 2. The occupation number of LUMO and the effective bond order (b_i) before spin projection change linearly with the orbital overlap. The n_i values are also calculated by using multi-configuration (MC) SCF, CASSCF and related multi-reference (MR) methods.

Unfortunately, at the moment, MR CI(CC) and related MR methods are hardly applicable to the geometry optimizations of the $CaMn_4O_5$ cluster (**1**) with hydrogen bonding networks in OEC of PSII, though they are really desirable. The nature of

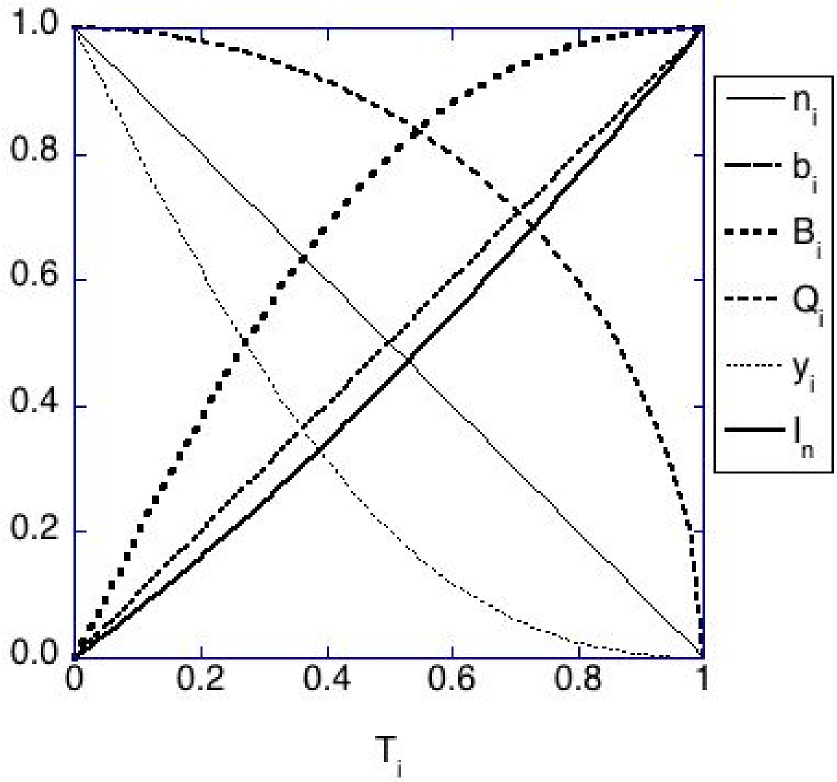

Figure S3 Functional behaviors of occupation number of LUMO, effective bond orders (b,B) before and after spin projection, information entropy (In), spin density index (Q) and diradical character (y) on variation of the orbital overlap (T).

chemical bonds in **1** can be explored from chemical indices described above that are commonly obtained by the analysis of density matrix of both BS and MR solutions. Therefore we have performed the natural orbital analysis of the UB3LYP solutions for the cluster to obtain natural orbitals and their occupation numbers that are utilized for derivation of chemical indices described above in refs. 36-44. Judging from several comparison between CASSCF natural orbitals and BS natural orbitals, their shapes (orbital-phase relations) are not so different, permitting qualitative discussions of shapes of LUMOs in relation to the electrophilicity of oxygen sites in the cluster as shown in ref. 37. The diradical character (y_i) is also calculated by using the orbital overlap (T_i) and the occupation number (n_i) as shown in refs. 36-43. We did not touch internal and semi-internal reductions of Mn(IV) ions of the $CaMn_4O_5$ cluster in previous papers (refs. 36-43) even though some of chemical indices have been obtained to elucidate labile nature of the high-valent Mn-O bonds. In fact, the internal and semi-internal reductions might not be discriminated from an external reduction discussed by Knapp.

SII.4 The internal reduction of high-valent Mn ions

Several papers published recently have examined the X-ray damage of the SP8 XRD structure as discussed in the text. However it should be careful to conclude such damage based on small cluster models without protein environments. Our computational results indicate the necessity of discrimination of the internal, semi-internal and external reductions of Mn ions to clarify the X-ray damage under current discussions. As shown in Fig. S3, the spin density can be used as a theoretical measure of the internal reduction of the high-valent Mn ions via the HOMO-LUMO mixing of the Mn-O bonds in eq. (s2). For example, let us consider the spin densities on the Mn ions in the low-spin (LS) configuration with the up(U)-up(U)-up(U)-up(U) spin alignment ($\uparrow\uparrow\uparrow\uparrow$) for the S_1 state. The spin densities obtained for S_{1R}(R) by the QM model I with the SP8 XRD structure are 4.47, 3.96, 3.83 and 3.80, respectively, for Mn_a, Mn_b, Mn_c and Mn_d. Therefore the valence states of Mn_a, Mn_b, Mn_c and Mn_d are assigned as III, III, III and III, in accord with the low-oxidation-model by Pace et al in refs. 52-55. This means that two Mn(IV) ions are reduced to two Mn(III) ions in consistent with the two-electron reduction state: S_{-1} state in the extended Kok cycle in Fig. S1 if the oxidation states of Mn ions are discussed. The XANES spectroscopy may detect the Mn(III) ions for this configuration.

However, the spin densities appear on the oxygen dianion sites of the Mn-O bonds as revealed by the natural orbital analysis in eqs. (s1) and (s2). The renormalized spin densities on the Mn ions are obtained by addition the spin densities on the oxygen dianions induced by the strong spin polarization (SP) effects as follows:

$$<Q\ (Mn_a)> = \quad 4.47\ ((Mn_a) - 0.71\ (O_{(4)}) = 3.76\ (III) \qquad (s21a)$$
$$<Q\ (Mn_b)> = \quad 3.96\ ((Mn_b) - 0.63\ (O_{(5)}) = 3.33\ (IV) \qquad (s21b)$$
$$<Q\ (Mn_c)> = \quad 3.83\ ((Mn_c)- 0.20(O_{(1)})-0.44(O_{(2)})-0.21(O_{(3)})= 2.98\ (IV) \qquad (s21c)$$
$$<Q\ (Mn_d)> = \quad 3.80\ ((Mn_d) = \quad 3.80\ (III) \qquad (s21d)$$

The normalized spin densities obtained by the QM model I with the XRD structure are 3.76, 3.33, 2.98 and 3.80, respectively, for Mn_a, Mn_b, Mn_c and Mn_d. Therefore the valence states of Mn_a, Mn_b, Mn_c and Mn_d are approximately assigned as III, IV, IV and III on the basis of the normalized spin densities. In fact, the sum of the absolute normalized spin densities is 13.9(16.0) where the corresponding value for the BS solution is given in parentheses. The sum of the absolute spin densities on the oxygen dianions is 2.2, providing the normalized value 13.8 (=16.0-2.2). This means that the reduction of the oxidation number of the Mn(IV) ion revealed by the BS computations is irrelevant to the external reduction by the X-ray radiation. Fortunately the normalized spin densities enabled us to derive the spin Hamiltonian model for the $CaMn_4O_5$ cluster of OEC of PSII by SP8 XRD has been as shown in section SII. 7 and refs. 36-44. More exact Huckel-Hubbard-Fund (HHH) models are desirable for more quantitative mapping of the computational results.

As discussed in the text, one of the practical methods to reduce the strong spin polarization effects is the full geometry optimization of the Mn-O bond lengths. Judging from the eq. (s21a) and (s21b), the Mn_a-$O_{(4)}$ and Mn_b-$O_{(3)}$ bond lengths should be shortened, respectively, to reduce the HOMO-LUMO mixing (spin polarization) in the full geometry optimization process. Similarly the Mn_c-$O_{(1)}$, Mn_c-$O_{(2)}$ and Mn_c-$O_{(3)}$ bond lengths are also shortened after the geometry optimization in conformity with eq. (21c). In fact, these bond lengths are shortened by 0.2-0.3 (Å) as compared with the corresponding SP8 XRD bond lengths after the full geometry optimizations as shown in refs. 41-44. As a result of reductions of these Mn-O bond lengths, the Mn-Mn distances are also shortened as compared with the corresponding SP8 XRD values. However the reduction of the Mn-Mn distance after the geometry optimization does not mean the external reduction of the cluster. It indicates some of elongated Mn-O distances of SP8 XRD are reduced by the full geometry optimizations.

The spin polarizations of the Mn-O bonds in eq. (s21) are partly reduced by inclusion of environmental effects of coordination water molecules and protein field as shown in the text and in Tables S1-S3. Therefore the reductions of the Mn-O and Mn-Mn bond lengths from the corresponding XRD values are suppressed as shown in Tables 1-2 in the text. Thus protein fields of the OEC of PSII suppress the SP effects that is expressed with reduction of the on-site repulsion U in the HHH model. However, QM Model III is still insufficient as a realistic model of OEC of PSII as discussed in the text. Therefore extension of our present QM/MM Models including many environmental species in Figs. 4-7 are inevitable for reliable discussions on the internal and semi-internal reductions of Mn(IV) ions that afford fundamental information for discussions of the remaining external reduction by X-ray radiation. Such extended QM/MM calculations are in progress in our group.

[S1] K. Yamaguchi, Int. J Quant Chem S14 (1980) 267.

[S2] K. Yamaguchi, In Self-Consistent Field Theory and Applications; Carbo, R.; Klobuskowski, G., Eds. Elsevier Scientific Pub: Amsterdam, 1990, p.727.

[S3] K. Yamaguchi, S. Yamanaka, M. Nishino, Y. Takano, Y. Kitagawa, H. Nagao and Y. Yoshioka, Theor. Chem. Acc, 102 (1999) 328.

[S4] H. Nagao, M. Nishino, Y. Shigeta, T. Soda, Y. Kitgawa, T. Onishi, Y. Yoshioka and K. Yamaguchi, Coord. Chem. Rev. 198 (2000) 265.
[S5] K. Yamaguchi, Chem. Phys. Lett. 33, 330 ; 35, 230 (1975).
[S6] K. Yamaguchi, Chem. Phys. Lett. 66, 395 (1979).
[S7] K. Yamaguchi, et al., AIP. Conf. Proc. 1108 (2009) 20.
[S8] K. Yamaguchi and T. Fueno, T. Chem. Phys. 19 (1978) 35.
[S9] K. Yamaguchi, Chem. Phys. 29 (1978) 117.
[S10] S. Yamanaka, S. Nishihara, K. Nakata, Y. Yonezawa, Y. Kitagawa, T. Kawakami, M. Okumura, T. Takada, H. Nakamura and K. Yamaguchi, in Recent Progress in Coupled Cluster Methods (P. Carsky et al Eds, 2010) 621.
[S11] Y. Takano, K. Yamaguchi, H. Nakamura, Biomimetic Based Applications, (A. George, Ed, In Teck 2011) Chaper 8 (p183-p200).

SII.5 Broken-symmetry solutions for CaMn$_4$O$_5$ cluster (1)

(A) Spin degree of freedom

First of all spin degree of freedom is examined. The broken-symmetry methods mentioned above have been applied to elucidate geometrical, electronic and spin structures of the CaMn$_4$O$_5$ cluster (**1**) in OEC of PSII,

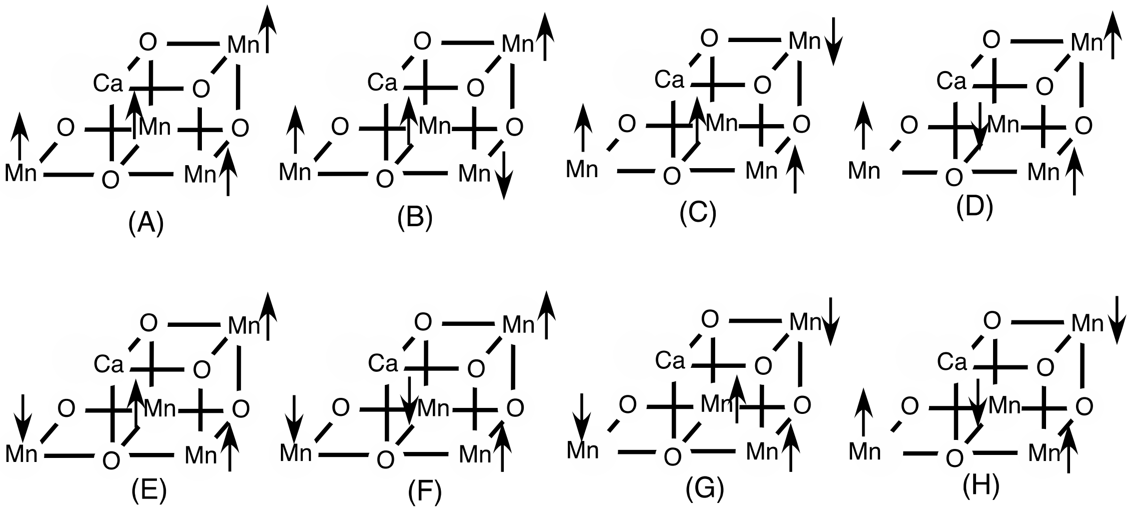

Figure S4 Eight broken-symmetry (BS) solutions for the CaMn$_4$O$_5$ cluster of OEC of PSII. These BS solutions are characterized using the spin vectors responsible for normalized spin densities discussed in section II. These are responsible for the spin degree of freedom under the BS approximation.

The HOMO-i and LUMO+i (i=0-7) mixings in eq. (s2) provides eight different broken-symmetry (BS) solutions that are characterized by spin densities. The spin densities are schematically expressed by the classical spin vector models as illustrated in the supporting Figure S4. The spin structure A with the parallel spin alignment expresses the highest spin (HS) configuration. The spin structures B, C, D and E denote the intermediate spin (IS) configurations. The spin structures F, G and H explain the low-spin (LS) configurations. Thus eight spin configurations arising from the spin degree of freedom are available for each mixed-valence (MV) state. The magnitude of spins (spin densities) in Fig. S4 are 5, 4 and 3 for Mn(II), Mn(III) and Mn(IV), respectively. However, the magnitude of spin densities obtained by the BS (QM and QM/MM) solutions are not integers because of spin polarizations and delocalizations as shown in Tables S1-S3. Nevertheless they are qualitatively consistent with the valence state II, III or IV, indicating an applicability of a localized spin model.

The spin densities for the high-spin HS(A) S_{1b}(R) ($O_{(5)}$=O^{-2}) state obtained by QM Model I with the XRD structure are 4.47, 3.96, 3.83 and 3.80, respectively, for Mn_a, Mn_b, Mn_c, and Mn_d as shown in the supporting Table S1. Therefore the valence state is qualitatively assigned to be III, III, III and III, respectively, as mentioned in section SII.4. This uniform valence structure is consistent with the low-oxidation-state model of the S_1 state in the refs. 52-54. In fact the sum of the spin densities of the manganese ions is 16.06. Therefore this configuration for the manganese ions is formally responsible for two-electron reduced state, namely S_{-1} state in the high-oxidation-state model for the extended Kok cycle in Fig. S1 as mentioned above (see SII.4). On the other hand, the spin densities on $O_{(1)}$, $O_{(2)}$, $O_{(3)}$, $O_{(4)}$ and $O_{(5)}$ are -0.20, -0.44, -0.21, -0.71 and -0.63, respectively. The sum of the spin densities of the oxygen dianions is -2.19. Therefore total spin density for the $CaMn_4O_5(H_2O)_4$ cluster is 13.9 (=16.06-2.19). This value is consistent with the S_1 valence state consisted of two Mn(III) and two Mn(IV) ions. Thus reductions of two Mn(IV) ions into two Mn(III) ions occur via spin polarization effects of the Mn(IV)-O bonds for the QM Model I with the XRD structure as formulated in section SII.4 (see equation (4) in the text). The $Mn(III)_4$ configuration does not mean the external reduction of the in the Mn(IV) ions. Here this type of reductions is referred to as an internal reduction of Mn ions. The internal two-electron reduction of the Mn(IV) ions is therefore different from the external two-electron reduction state obtained by addition of extra two electrons to the CaMn4O5 cluster: this corresponds to the true S_{-1} valence state consisted of four Mn(III) ions. This is the reason why we did not touch the radiation damage based on the small QM model I without full geometry optimization in our early papers (refs.

36-41).

The spin densities for the HS(A) S_{1b} state obtained by the full geometry optimization (OPT) of the QM Model I are 3.85, 2.93, 2.96 and 3.84, respectively, for Mn_a, Mn_b, Mn_c, and Mn_d as shown in Table S1. Therefore the valence state is qualitatively assigned to be III, IV, IV and III, respectively. In fact the sum of the spin densities of the manganese ions is 13.6. Therefore this configuration for the manganese ions is responsible for the S_1 state in the high-oxidation-state scenario. On the other hand, the spin densities on $O_{(1)}$, $O_{(2)}$, $O_{(3)}$, $O_{(4)}$ and $O_{(5)}$ are 0.03, 0.02, 0.01, 0.05 and 0.06, respectively. The sum of the spin densities of the oxygen dianions is 0.17. Therefore total spin density for the $CaMn_4O_5(H_2O)_4$ cluster is 13.8 (=13.58+0.17). This value is consistent with the S_1 valence state consisted of two Mn(III) and two Mn(IV) ions. Thus internal reductions of two Mn(IV) ions into two Mn(III) ions disappear after the full geometry optimizations of the QM Model I. Thus discrimination between internal and external reductions of Mn (IV) ions is crucial for theoretical understanding of the nature of the chemical bonds of the high-valent manganese oxides such as the $CaMn_4O_5(H_2O)_4$ cluster of OEC of PSII.

How about the internal reduction in the low-spin states? The spin densities for the low-spin LS(↓↑↓↑) S_{1b} state obtained by QM(Model II)/MM model with the XRD structure are -4.26(4.27), 3.84(-3.87), -3.70(-3.70) and 3.83(3.81), respectively, for Mn_a, Mn_b, Mn_c, and Mn_d as shown in the supporting Table S1, where the corresponding values LS(↑↓↓↑) S_{1b} state are given in parentheses. The valence state for both LS configurations is qualitatively assigned to be III, III, III and III, respectively, even in the QM/MM model, in accord with the low-oxidation-state model in refs. 52-55. In fact the sum of the absolute spin densities of the manganese ions is 15.6(15.7). Therefore this configuration for the manganese ions is approximately responsible for the S_{-1} state though the internal reduction decreases by 0.5 by the hydrogen bonding as compared with that of QM Model I. The spin densities on $O_{(1)}$, $O_{(2)}$, $O_{(3)}$, $O_{(4)}$ and $O_{(5)}$ are 0.10(0.09), 0.26(0.36), 0.06(0.14), 0.37(-0.23) and -0.80(0.83), respectively. The sum of the absolute spin densities of the oxygen dianions is 1.59(1.65). The total spin density for the $CaMn_4O_4(HO)_2(H_2O)_3$ cluster becomes 14.0 (14.0). This value is consistent with the S_1 valence state consisted of two Mn(III) and two Mn(IV) ions. Thus the spin polarization (SP) effects for the Mn(IV)-O bonds did not disappear even by the QM/MM model under the assumption of SP8 XRD geometry. Thus relatively small QM region (QM Model I plus seven water molecules) is not sufficient enough for quantitative discussions of the internal reduction of Mn(IV) ions. This in turn means that the full geometry optimizations are necessary for reduction of the SP effects in this level of the QM/MM computations.

The spin densities for the LS(↓↑↓↑) S_{1b} state obtained by the full geometry optimization (OPT) of the QM(Model II)/MM model are -3.88(3.89), 2.89(-2.88), -2.96(-2.98) and 3.87(3.86), respectively, for Mn_a, Mn_b, Mn_c, and Mn_d where the corresponding values for LS(↑↓↓↑) S_{1b} state are given in parentheses. The sum of the absolute spin densities of the manganese ions is 13.6(13.6). On the other hand, the spin densities on $O_{(1)}$, $O_{(2)}$, $O_{(3)}$, $O_{(4)}$ and $O_{(5)}$ are 0.02(-0.04), -0.02(0.04), -0.03(0.01), 0.11(-0.10) and 0.03(-0.05), respectively. The sum of the spin densities of the oxygen dianions is 0.11(0.16). Therefore total spin density for the $CaMn_4O_4(HO)_2(H_2O)_3$ cluster after the geometry optimization is 13.7 (13.8). This value is consistent with the S_1 valence state consisted of two Mn(III) and two Mn(IV) ions. Thus the valence configuration of the S_1 state by the SP8 XRD structure is well reproduced by the full geometry optimization of the QM(Model II)/MM model.

The SP8 XRD structure does not elucidate the positions of hydrogen atoms. The spin density on the $O_{(5)}$ site of the S_{1b} model ($O_{(5)}$=O^{2-}) is significantly large, indicating the radical reactivity of this site. This in turn indicates the possibility of its protonation ($O_{(5)}$=OH^-). The spin densities for the low-spin LS(↓↑↓↑) S_{1a} state ($O_{(5)}$=OH^-) obtained by QM(Model II)/MM model with the XRD structure are -4.19, 3.85, -3.87 and 3.69, respectively, for Mn_a, Mn_b, Mn_c, and Mn_d as shown in the supporting Table S1. The valence state for S_{1a}(R) is qualitatively assigned to be III, III, III, III in the QM/MM model. In fact the sum of the absolute spin densities of the manganese ions is 15.6. The spin densities on $O_{(1)}$, $O_{(2)}$, $O_{(3)}$, $O_{(4)}$ and $O_{(5)}$ are 0.10, 0.25, 0.07, 0.50 and -0.06, respectively, whereas the spin density on the HO group coordinated to $Mn_{(a)}$ is 0.23. The spin density on the $O_{(5)}$ site almost disappears by its protonation in accord with the computational models by Knapp et al. [50,51] Therefore the sum of the spin densities of the oxygen dianions is 1.09. This means that the internal reduction is approximately 1, affording the S_0 state in contradiction to the case of QM Model I that predicts the the S_{-1} state.

Where is one more hole? Interestingly it is on the His337 since the charge transfer (CT) from His337 to $Mn_{(b)}$ is -0.57. Here such partial reduction of Mn_b ion by the CT from amino acid residues in second-coordination shell is referred to as the semi-internal reduction. The renormalized spin densities on the Mn ions are

$$\langle Q\,(Mn_a)\rangle = -4.19\,(Mn_a) + (0.50-0.20)\,(O_{(4)}) = -3.89\ (\mathrm{III}) \qquad (s22a)$$

$$\langle Q\,(Mn_b)\rangle = 3.85\,(Mn_b) - 0.57\,(\mathrm{His337}) - 0.06\,(O_{(5)}) = 3.22\ (\mathrm{IV}) \qquad (s22b)$$

$$\langle Q\,(Mn_c)\rangle = -3.87(Mn_c) + 0.10(O_{(1)}) + 0.25(O_{(2)}) + 0.07(O_{(3)})$$

$$+ 0.20(O_{(4)}) = -3.25 \text{ (IV)} \qquad \text{(s22c)}$$

$$\langle Q\ (Mn_d) \rangle = \quad 3.81\ ((Mn_d) = 3.81 \text{ (III)} \qquad \text{(s22d)}$$

obtained by addition of these spin densities on the basis of the natural orbital analysis. QM Model II does not involve explicitly His337 which is stabilized with hydrogen bond of its nitrogen atom with water molecule. QM Model II is still insufficient for quantitative purpose, The present results in turn indicates that the full geometry optimizations based on the QM(QM Model II)/MM model are desirable even for qualitative discussions of the X-ray damage of SP8 XRD for the OEC of PSII as shown in this paper.

The full geometry optimizations are inevitable for avoiding the internal reduction of the high-valent Mn(IV) ions in our present QM models even for the S_0 state. The spin densities for the right-elongated LS(↑↓↑↓) S_{0a}(R) state obtained by the full geometry optimization of the QM Model III are 4.75(3.93), -2.71(-3.83), 3.05(2.93) and -3.88(3.85), respectively, as shown in Table S2, where the corresponding values for IS(↑↓↑↑) by the QM/MM model are given in parentheses. Therefore the valence state is assigned to be II(III), IV(III), IV and III as discussed in the text. The sum of the absolute spin densities is 14.4(14.4): note that the formal sum of the absolute spin densities is 15.0 for the S_0 state. On the other hand, spin densities for the left-elongated LS(↓↑↓↑) S_{0a}(L) state obtained by QM(Model II)/MM are 4.75(3.98), -2.71(3.88), 3.05(3.13) and -3.88(-3.87), respectively, as shown in Table S2, where the corresponding values for IS(↑↑↑↓) by the QM/MM model are given in parentheses. Therefore the valence state is assigned to be II(III), IV(III), IV(IV) and III(III). The sum of the absolute spin densities is 14.4 (14.9). The internal and semi-internal reductions of Mn ions are almost zero in the case of both right- and left-elongated optimized structures in the S_0 state.

The spin densities for the LS(↓↑↓↑) S_{1a}(R) state obtained by the full geometry optimization of the QM Model III are -3.88(-3.88), 2.89(2.90), -2.96(-2.97) and 3.87(3.87), respectively, as shown in Table S3, the corresponding values for the optimized hydrogen-bond network (eleven water molecules) for the S_0 state are given in the parentheses. Therefore the valence state is assigned to be III, IV, IV and III as discussed in the text. The sum of the absolute spin densities is 13.6(13.6), indicating the S_1 state in the high-oxidation scenario. The spin densities for the IS(↑↑↑↓) S_{1a}(R) state obtained by the full geometry optimization of the QM Model III are 3.97, 2.86, 3.03 and -3.90, respectively, as shown in Table S3. Therefore the valence state is also assigned to be III, IV, IV and III as discussed in the text. The sum of the absolute spin densities is 14.0, indicating the S_1 state in the high-oxidation scenario.

The spin densities for the LS(↓↑↓↑) S_{1a}(L) state obtained by the full geometry optimization of the QM Model III are -3.89(-3.88), 2.86(2.94), -3.03(-3.03) and 3.90(3.89), respectively, as shown in Table S3, the corresponding values for the optimized hydrogen-bond network (eleven water molecules) for the S_0 state are given in the parentheses. Therefore the valence state is assigned to be III, IV, IV and III as discussed in the text. The sum of the absolute spin densities is 13.7(13.7), indicating the S_1 state in the high-oxidation scenario. The spin densities for the LS(↑↓↓↑) S_{1a}(R) obtained by the full geometry optimization of the QM Model III are 3.92, -2.85, -3.02 and 3.90, respectively, as shown in Table S3. Therefore the valence state is also assigned to be III, IV, IV and III as discussed in the text. The sum of the absolute spin densities is 13.7, indicating the S_1 state in the high-oxidation scenario. Thus the valence configurations of the optimized QM Model III are normal without significant internal reductions of Mn(IV) ions. It is noteworthy that small reductions of the Mn-Mn, Ca-Mn and Mn-O distances of SP8 XRD by the full geometry optimizations provide these reasonable results.

The spin densities obtained by the broken-symmetry (BS) UB3LYP calculations indicate the valence configurations with local spins II, III or IV, indicating the applicability of the spin Hamiltonian model as shown in section SII.7. The effective exchange integrals in the spin Hamiltonian model are obtained by the energy difference among total energies of eight BS solutions as shown previously.[38,41,43] The spin Hamiltonian models are used to perform approximate spin projections for the BS energy levels. The spin Hamiltonian models are also diagonalized exactly to elucidate the energy levels which are used for theoretical analysis of magnetic properties of the transition-metal clusters revealed by ESR, ENDOR, etc as shown previously.[72] This in turn indicates that detailed analysis of the ESR results for the SP8 XRD crystal of OEC of PSII by Umena et al[34,35] may provide useful information of its electronic and spin states.

The present QM(QM Model II)/MM computational results have indicated the significant reductions of Mn ions in the SP8 XRD structure. This clearly indicates the necessity of inclusion of other molecules as shown in Figs. 4-7 in the text for quantitative discussions of both internal and semi-internal reductions of the high-valent Mn ions in OEC of PSII. For example, judging from the computational results in Tables S1-S3 more reliable models are conceivable as follows: QM(QM Model III)/MM and QM Model IV(OM Model III plus other waters and amino acid residues in Figs. 4-7)/MM models. These model computations are in progress. Therefore it is too early to conclude the external radiation damage of the SP8 XRD structure based on the optimized QM model calculations without such environmental effects of protein. We feel that relatively large QM models are necessary for quantitative discussions of redox active systems such as OEC of PSII.

Table S1 Spin populations on the Ca, Mn and O atoms for the XRD and right(R)-elongated optimized structures in the S1 state obtained by the UB3LYP calculations based on the QM model I and QM(model II)/MM model.

Atom	S_{1b}(C)		$S_{1b(a)}$(R)	
	HS(UUUU)[a)]	HS(UUUU)[b)]	LS(DUDU)[c)]	LS(DUUD)[d)]
Ca	-0.02	0.00	0.00(0.00)[0.00]	0.01(-0.01)
Mn_a	4.47	3.85	-4.26(-3.88)[-4.19]	4.27(3.89)
Mn_b	3.96	2.93	3.84(2.89)[3.85]	-3.87(-2.88)
Mn_c	3.83	2.96	-3.70(-2.96)[-3.87]	-3.70(-2.98)
Mn_d	3.80	3.84	3.83(3.87)[3.69]	3.81(3.86)
$O_{(1)}$	-0.20	0.03	0.14(0.02)[0.06]	0.09(-0.04)
$O_{(2)}$	-0.44	0.02	0.26(-0.02)[0.25]	0.36(0.04)
$O_{(3)}$	-0.21	0.01	0.06(-0.03)[0.07]	0.14(0.01)
$O_{(4)}$	-0.71	0.05	0.37(0.11)[0.50]	-0.23(-0.10)
$O_{(5)}$	-0.63	0.06	-0.80(0.03)[-0.06]	0.83(-0.05)

[a)] QM Model I (XRD, O(5)=O^{2-}):HS(↑↑↑↑), [b)] Model I (OPT, O(5)=O^{2-}): HS(↑↑↑↑), [c)] QM/MM Model (XRD) LS(↓↑↓↑)(QM/MM Model (OPT) LS(↓↑↓↑) values in parentheses ( ) and QM/MM Model (XRD, O(5)=OH^-) LS(↓↑↓↑) values in parentheses [ ]), [d)] QM/MM Model (XRD) LS(↑↓↓↑)(QM/MM Model (OPT) LS(↑↓↓↑) values in parentheses) . The spin densities for a) and b) are taken from the refs. 39 and 41.

Table S2 Spin populations on the Ca, Mn and O atoms for the left (L)- and right(R)-elongated optimized structures in the S0 state obtained by the UB3LYP calculations based on QM model III.

Atom	S_{0a}(L)		S_{0a}(R)	
	LS(UDUD)a)	LS(UDUD)b)	LS(UDUD)c)	IS(UUUD)d)
Ca	0.00	-0.00	0.00	0.01
Mna	4.75	3.83	4.75	3.98
Mnb	-2.71	-3.83	-2.71	3.88
Mnc	3.05	2.93	3.05	3.13
Mnd	-3.88	3.85	-3.88	-3.87
O(1)	0.00	0.02	0.00	-0.02
O(2)	-0.04	-0.04	-0.04	-0.07
O(3)	0.03	-0.02	0.03	-0.02
O(4)	-0.26	0.02	-0.25	-0.10
O(5)	0.05	0.00	0.05	0.07

a) Model III (O(5)=OH$^-$, W$_{(2)}$ = H$_2$O): LS(↑↓↑↓) , b)QM/MM Model (O(5)=OH$^-$, W$_{(2)}$=H$_2$O) LS(↑↓↑↓) ,c)Model III: (O(5)=OH$^-$,W$_{(2)}$=H$_2$O):LS(↓↑↓↑) , d)Model III (O(5)=OH$^-$, W$_{(2)}$ = H$_2$O) :LS(↑↑↑↓)

Table S3 Spin populations on the Ca, Mn and O atoms for the left (L)- and right(R)-elongated optimized structures in the S1 state obtained by the UB3LYP calculations

.

Atom	S_{1a}(L)		S_{1a}(R)	
	LS(DUDU)a)	LS(UDDU)b)	IS(UUUD)c)	LS(DUDU) d)
Ca	0.01 (0.01)	-0.01	0.01	0.00(-0.01)
Mna	-3.89 (-3.88)	3.92	3.97	-3.88 (3.88)
Mnb	2.86 (2.94)	-2.85	3.11	2.89(-2.90)
Mnc	-3.03(-3.03)	-3.02	3.05	-2.96 (2.97)
Mnd	3.90(3.89)	3.90	-3.86	3.87 (3.87)
O(1)	-0.02(-0.02)	-0.02	0.00	0.01(0.00)
O(2)	0.05(0.05)	0.03	-0.05	-0.02(0.03)
O(3)	-0.05(-0.05)	-0.01	-0.01	-0.03(0.01)
O(4)	0.18(0.13)	-0.17	0.06	0.11(-0.08)
O(5)	-0.05(-0.05)	0.09	-0.02	0.03(-0.01)

a)Model III (O(5)=OH^- , $W_{(2)}$ = H_2O):LS(↓↑↓↑)(values by Net(S0) is given in parentheses) , b)Model III(O(5)=OH^- , $W_{(2)}$ = H_2O) LS(↑↓↓↑),c)Model III (O(5)=OH^- , $W_{(2)}$ = H_2O) : IS(↑↑↑↓),d) QM/MM (O(5)=OH^- , $W_{(2)}$ = H_2O) : LS(↓↑↓↑) (values by LS(↑↓↓↑) in parentheses).

(B) Charge degree of freedom

The S_1 state of the $CaMn_4O_5$ cluster is composed of two Mn(III) and two Mn(IV) ions as shown in the supporting Figure S5. Therefore six different mixed-valence (MV) configurations are available from the charge degree of freedom. Thus total 8x6=48 broken-symmetry solutions are feasible in the S_1 state as shown previously (ref. 36,39). The optimized geometries are variable, depending the MV configurations as shown in ref. 39-43. On the other hand, four different MV configurations are available for the three Mn(III)-one Mn(IV)(S_0 state) system, three Mn(IV)-one Mn(III) (S_2 state) system and three Mn(IV) and one Mn(V) (S_4 state) system in the Kok cycle in Fig. S1. Only one MV configuration is feasible for the uniform valence systems $Mn(III)_4$ (S_{-1} state) and $Mn(IV)_4$ (S_3 state). The calculated energy differences among several different MV configurations are not so large, indicating that electron hopping is feasible in accord with labile nature of chemical bonds in **1**. These hole-doped Mott insulating.

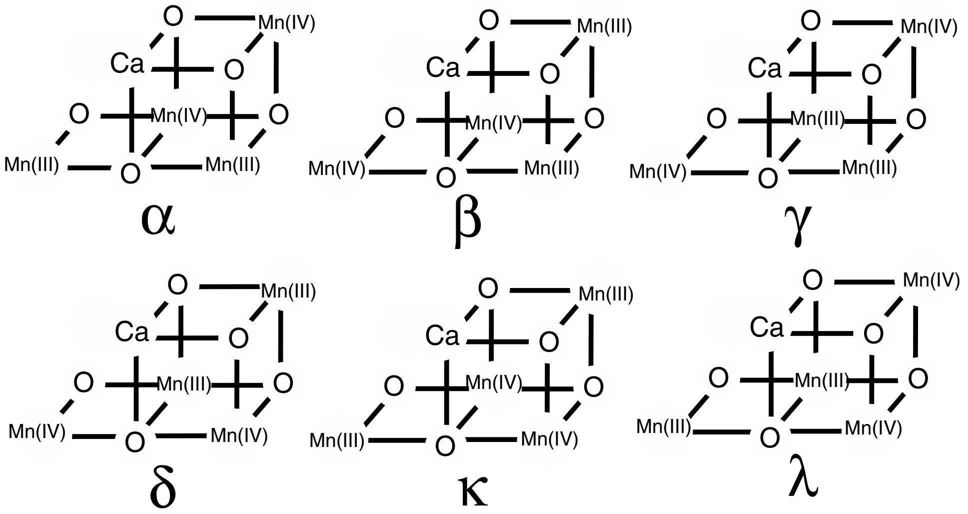

Figure S5 Six different mixed-valence (MV) configuration for the S1 state of the $CaMn_4O_5$ cluster consisted of $Mn(III)_2$ and $Mn(IV)_2$ ions. These are responsible for charge degree of freedom.

states play important roles for water oxidation as discussed in our previous papers (refs. 36-44).

(C) Orbital degree of freedom

The orbital degree of freedom in the Mn(III) ion provides the Jahn-Teller (JT) distortion of the $CaMn_4O_5$ cluster (**1**) as shown in the supporting Figure S2. The JT effects act effectively the suppression and/or elongation of the Mn-O bonds, affording the left (L)- and right (R)-elongated structures as shown previously (see Fig. S2).[42] Such elongations also entail the possibility of water insertion into a coordination unsaturated site as illustrated in the Figure S2. Previously the right (R)-elongated structure has been discussed in the magnetic spectroscopy[24-31] of the S_2 state of the $CaMn_4O_5$ cluster (**1**). However, previous[42] and present computational results indicate that energy differences between L and R type geometrical isomers are not so large, indicating flexibility of **1**.

Thus spin, charge and orbital degrees of freedom play important roles for understanding of the nature of chemical bonds of the $CaMn_4O_5$ cluster (**1**). This is consistent with our theoretical picture[68,72] that **1** is a typical example of strongly correlated electron systems (SCES) like the hole-doped Ln2CuO4 in the high-Tc superconducting systems: extremely difficult system indeed. We have performed systematic theoretical studies of possible variations of the cluster based on these freedoms as summarized in the next section.

SII.6 Developments of theoretical studies on water oxidations

The broken-symmetry (BS) density functional theory (DFT) methods have been applied to elucidate geometrical, electronic and spin structures of the $CaMn_4O_5$ cluster of OEC of PSII starting from the SP8 XRD structure discovered by Umeya, Kawakami, Shen, Kamiya (ref. 34): title of their paper is given by

Crystal structure of oxygen-evolving photosystem II at a resolution of 1.9 Å (Nature, 2011, 473, 55-60, ref. 34 in the text).

Present UB3LYP calculations have been performed to elucidate scope and applicability of the working hypotheses WH1-WH11. Possible reaction mechanisms for water oxidation at OEC of PSII are also examined on the XRD structure and the calculated results. However the length of the supporting materials becomes too long if such parts are reproduced here. Therefore the titles of our theoretical papers are cited for readers in the fields of catalytic science as follows:

S1(Ref 36)

Labile electronic and spin states of the $CaMn_4O_5$ cluster in the PSII systems refined to the 1.9 Å X-ray resolution. UB3LYP computational results
K. Kanda, S. Yamanaka, T. Saito, Y. Umena, K. Kawakami, J. R. Shen, N. Kamiya, M. Okumura, H. Nakamura, K. Yamaguchi, Chem. Phys. Lett. 2011, **506**, 98-103.

S2(Ref 37)

Possible mechanisms for the O-O bond formation in oxygen evolution reaction at the $CaMn_4O_5(H_2O)_4$ cluster of PSII refined to the 1.9 Å X-ray resolution
S. Yamanaka, H. Isobe, K. Kanda, T. Saito, Y. Umena, K. Kawakami, J. R. Shen, N. Kamiya, M. Okumura, H. Nakamura, K. Yamaguchi, K. Chem. Phys. Lett. 2011, **511**, 138-145.

S3(Ref 38)

Possible mechanisms of water splitting reactions based on proton and electron release pathways revealed for $CaMn_4O_5$ cluster of PSII refined to the 1.9 Å X-ray resolution
T. Saito, S. Yamanaka, K. Kanda, H. Isobe, Y. Takano, Y. Shigeta, Y. Umena, K. Kawakami, J. R. Shen, N. Kamiya, M. Okumura, M. Shoji, Y. Yoshioka, K. Yamaguchi, Int. J. Quant. Chem. 2012, **112**, 253-276.

S4(Ref 39)

Structure and reactivity of the mixed-valence $CaMn_4O_5(H_2O)_4$ and

$CaMn_4O_4(OH)(H_2O)_4$ clusters at oxygen evolution complex of photosystem II. Hybrid DFT (UB3LYP and UBHandHLYP) calculations

S. Yamanaka, T. Saito, K. Kanda, H. Isobe, Y. Umena, K. Kawakami, J. R. Shen, N. Kamiya, M. Okumura, H. Nakamura, K. Yamaguchi, Int. J. Quant. Chem. 2012, **112**, 321-343.

S5(Ref 40)

Full geometry optimizations of the mixed-valence $CaMn_4O_4X(H_2O)_4$ (X=OH or O) cluster in OEC of PS II: Degree of symmetry breaking of the labile Mn-X-Mn bond revealed by several hybrid DFT calculations

K. Yamaguchi, S. Yamanaka, T. Saito, K. Kanda, H. Isobe, M. Shoji, Y, Umeya, K. Kawakami, J. R. Shen, N. Kamiya, M. Okumura, Int. J. Qunat, Chem, DOI: 10.1002/qua.24117, **2013**, 113, 525-541.

S6(Ref 41)

The nature of chemical bonds of the $CaMn_4O_5$ cluster in oxygen evolving complex of photosystem II: Jahn-Teller distortion and its suppression of Ca doping in cubane structures

K. Yamaguchi, S. Yamanaka, H. Isobe, T. Saito, K. Kanda, Y, Umeya, K. Kawakami, J. R. Shen, N. Kamiya, M. Okumura, H. Nakamura, M. Shoji, Y. Shoshioka, Int. J. Qunat, Chem, DOI: 10.1002/qua.24280, **2013**, 113, 453-473. .

S7(Ref 42)

Theoretical illumination of water-inserted structures of the $CaMn_4O_5$ cluster in the S2 and S3 states of oxygen-evolving complex of photosystems II: full geometry optimizations by B3LYP hybrid density functional

H. Isobe, M. Shoji, S. Yamanaka, Y. Umena, K. Kawakami, N. Kamiya, J. –R. Shen, K. Yamaguchi, Dalton Trans. 2012, **41**, 13727-13740.

S8(Ref 43)

Electronic and spin structures of the $CaMn_4O_5(H_2O)_4$ cluster in OEC of PSII refined to the 1.9 Å X-ray resolution

S. Yamanaka, K. Kanda, T. Saito, Y. Umena, K. Kawakami, J. –R. Shen, N. Kamiya, M. Okumura, H. Nakamura, K. Yamaguchi, Adv. Quant. Chem. 2012, Vol 64, 121-187.

S9(Ref 44)

Theory of chemical bonds in metalloenzymes-Manganese oxysides clusters in the oxygen evolving center

K. Yamaguchi, M. Shoji, T. Saito, H. Isobe, S. Yamada, S. Nishihara, T. Kawakami,

Y. Kitagawa, S. Yamanaka, M. Okumura, AIP Conf. Proc. **2012**, 1504, 63-79.

SII. 7. A common theoretical picture for the native and artificial water oxidation systems based on the model Hamiltonian

Theoretical computations of OEC of PSII are expected to provide guiding principles for rational design of artificial catalysts for water oxidation. Broken-symmetry (BS) methods indeed provide a useful concept, namely isolobal and isospin analogy, for molecular design of artificial photocatalysts for water oxidation. The broken-symmetry (BS) DFT calculations on the native $CaMn_4O_5$ cluster of OEC of PSII and artificial Ru-semiquinone complexes have elucidated a common theoretical picture between the native and artificial water oxidation systems on the basis of the effective spin Hamiltonian model derived in refs. 38-44. The BS computational results have also elucidated a basic concept, namely the isolobal and isospin analogy, for molecular design of artificial catalysts for water oxidation.

Magnetic measurements provide experimental information to elucidate scope and applicability of the BS methods. Therefore, BS computational results are mapped into the Heisenberg spin Hamiltonian model that is conveniently utilized for characterization of spin degree of freedom in ESR, ENDOR, etc. The magnetic measurements have been performed for a number of exchange coupled systems such the native $CaMn_4O_5$ cluster. The Heisenberg spin Hamiltonian model has been employed for analysis of the experimental results available. In order to elucidate similarity between CaMn4O5 and artificial systems with four spin sites we here consider the model Hamiltonian for four-site four spin systems. The Heisenberg spin Hamiltonian for the systems is given by (refs. 38-43)

$$\begin{aligned}
\mathbf{H} &= -2J_{ab}\mathbf{S}_a\cdot\mathbf{S}_b - 2J_{ac}\mathbf{S}_a\cdot\mathbf{S}_c - 2J_{ad}\mathbf{S}_a\cdot\mathbf{S}_d - 2J_{bc}\mathbf{S}_b\cdot\mathbf{S}_c - 2J_{bd}\mathbf{S}_b\cdot\mathbf{S}_d - 2J_{cd}\mathbf{S}_c\cdot\mathbf{S}_d \\
&= -J_{ab}[(\mathbf{S}_a+\mathbf{S}_b)^2 - \mathbf{S}_a{}^2 - \mathbf{S}_b{}^2] - J_{ac}[(\mathbf{S}_a+\mathbf{S}_c)^2 - \mathbf{S}_a{}^2 - \mathbf{S}_c{}^2] - J_{ad}[(\mathbf{S}_a+\mathbf{S}_d)^2 - \mathbf{S}_a{}^2 - \mathbf{S}_d{}^2] \\
&\quad -J_{bc}[(\mathbf{S}_b+\mathbf{S}_c)^2 - \mathbf{S}_b{}^2 - \mathbf{S}_c{}^2] - J_{bd}[(\mathbf{S}_b+\mathbf{S}_d)^2 - \mathbf{S}_b{}^2 - \mathbf{S}_d{}^2] - J_{cd}[(\mathbf{S}_c+\mathbf{S}_d)^2 - \mathbf{S}_c{}^2 - \mathbf{S}_d{}^2] \\
&= -J_{ab}\mathbf{S}_{ab}{}^2 - J_{ac}\mathbf{S}_{ac}{}^2 - J_{ad}\mathbf{S}_{ad}{}^2 - J_{bc}\mathbf{S}_{bc}{}^2 - J_{bd}\mathbf{S}_{bd}{}^2 - J_{cd}\mathbf{S}_{cd}{}^2 \\
&\quad +\mathbf{S}_a{}^2(J_{ab}+J_{ac}+J_{ad}) + \mathbf{S}_b{}^2(J_{ab}+J_{bc}+J_{bd}) + \mathbf{S}_c{}^2(J_{bc}+J_{cd}+J_{ac}) + \mathbf{S}_d{}^2(J_{cd}+J_{ad}+J_{bd})
\end{aligned}$$

(s23)

where $\mathbf{S}_i$ means the spin operator, and the sum of the spin operators is defined by

$$\mathbf{S}_{ij} = \mathbf{S}_i + \mathbf{S}_j, \mathbf{S}_i = local\ spin\ on\ Ru\ and\ quinone \qquad \text{(s24)}$$

Therefore the expectation value for the spin Hamiltonian is given on the quantum mechanics as

$$\begin{aligned}<\mathbf{H}>_Q = &-J_{ab}S_{ab}(S_{ab}+1) - J_{ac}S_{ac}(S_{ac}+1) - J_{ad}S_{ad}(S_{ad}+1)\\ &-J_{bc}S_{bc}(S_{bc}+1) - J_{bd}{}^{2}S_{bd}(S_{bd}+1) - J_{cd}S_{cd}(S_{cd}+1)\\ &+S_a(S_a+1)(J_{ab}+J_{ac}+J_{ad}) + S_b(S_b+1)(J_{ab}+J_{bc}+J_{bd})\\ &+S_c(S_c+1)(J_{bc}+J_{cd}+J_{ac}) + S_d(S_d+1)(J_{cd}+J_{ad}+J_{bd})\end{aligned} \qquad \text{(s25)}$$

where S_i and S_{ij} are spin quantum numbers of quantum spin i and spin pair (ij), respectively. J_{ab} denotes the effective exchange integral between sites a and b that is given by the average of orbital contributions i and j. The J_{ab} values can be determined by the electron spin resonance (ESR) and other magnetic measurements.

The expectation values of the Heisenberg spin Hamiltonian are often approximated on the assumption that local spins are regarded as classical (axial) spin (vector). Here the up- and –down spin vectors are considered in accord with broken-symmetry (BS) calculations of the different-orbitals-for-different-spins (DODS) type. Then the expectation values of the classical Heisenberg model are given by

$$\begin{aligned}<\mathbf{H}>_C = &-J_{ab}S_{ab}{}^{2} - J_{ac}S_{ac}{}^{2} - J_{ad}S_{ad}{}^{2} - J_{bc}S_{bc}{}^{2} - J_{bd}{}^{2}S_{bd}{}^{2} - J_{cd}S_{cd}{}^{2}\\ &+S_a{}^{2}(J_{ab}+J_{ac}+J_{ad}) + S_b{}^{2}(J_{ab}+J_{bc}+J_{bd})\\ &+S_c{}^{2}(J_{bc}+J_{cd}+J_{ac}) + (J_{cd}+J_{ad}+J_{bd})\end{aligned} \qquad \text{(s26)}$$

Figure S4 illustrates possible spin alignments of four spin vectors. The total energies of the eight different BS DFT solutions are used to determine the effective exchange integrals (J) in eq. (s24)-(s26). Thus four spin systems for four one-electron transfers are commonly described by the spin Hamiltonian model. The above spin Hamiltonian model has been applied to elucidate a common theoretical picture between the native oxidation system $CaMn_4O_5$ cluster and Tanaka catalyst. As mentioned above, the normalized spin densities were used for derivations of the spin Hamiltonian model for the SP8 XRD structures where the internal reduction of high-valent Mn(IV) is is significant in the case of its small QM models, though such internal reductions disappear after the full geometry optimizations. The titles of our theoretical papers for rational design of artificial catalysts for water oxidation are given as follows:

S10(Ref 75)

Similarities of artificial photosystems by ruthenium oxo complexes and native water splitting systems

K. Tanaka, H. Isobe, S. Yamanaka, K. Yamaguchi, Proc. Natl. Acad. Sci. 2012, 109, 15600-15605.

S11(Ref 76)

Spin Hamiltonian models for artificial and native water splitting systems Revealed by hybrid DFT calculations. Oxygen activation by high-valent Mn and Ru ions

K. Yamaguchi, S. Yamanaka, H. Isobe, K. Tanaka, N. Ueyama, Int. J. Qunat, Chem, DOI: 10.1002/qua.24270, **2012**, 112, 3849-3866.

SIII. QM/MM method for biological systems

Quantum mechanical (QM) calculations based on the broken-symmetry (BS) DFT theoretical models are useful enough for theoretical illumination of essential features of electronic and spin states of the $CaMn_4O_5$ cluster of OEC of PSII that has a typical strongly correlated electron system (SCES) consisted of 3d electrons of Mn ions (ref. 71). However, as shown in our book (ref. 68), characteristics of metalloenzymes are regarded as confined states of SCES (refs. 71 and 72) with proteins. The confinement effects are indeed considered to be important for constructions of complex geometrical structures of metalloenzymes. Moreover hydrogen-bonding interactions act effectively for regulation of functional behaviors in the confined state. As a continuation of previous QM calculations in section SII, we have examined the effects for the $CaMn_4O_5$ cluster of OEC of PSII.

One of the theoretical methods for elucidation of the confinement effects (ref. 66) is the QM/molecular mechanics (MM) method initiated by Warshel and Levitt. (ref. S12). Over the past decades, a number of QM/MM calculations have been performed to elucidate mechanisms of enzymatic reactions. The QM/MM approach is now established as a valuable tool for theoretical modeling of biological reactions. Recently Senn and Thiel (ref. S13) have written a comprehensive review article concerning with the QM/MM calculations in biomolecular systems. Here, an essential feature of the QM/MM method is described in relation to our present calculations of OEC of PSII, where previous QM model (Model I in the text) plus seven coordinated water molecules is employed as an extended QM model (Model II in the text) and the remaining part is investigated with the MM method.

In the QM/MM method the entire system (**S**) is partitioned into the inner region (**I**) that is treated quantum-mechanically and the other outer region (**O**) is described by a highly efficient force field. Therefore the inner (**I**) and outer (**O**) regions are referred to as QM and MM regions, respectively. However, owing to the QM-MM interactions, the total energy of the entire system cannot simply be written as the sum of the energies of the subsystems, indicating an importance of the boundary region between the QM and MM parts. In this paper we have employed a standard link (**L**) atom model that caps the QM subsystem treated by the DFT SCF method. Detalis of QM model of amino acid residues are given in the text. AMBER force field is used for the present MM calculations. An additive QM/MM scheme has been employed because no reliable force fields are available for Mn ions in the $CaMn_4O_5$ cluster.

The basic energy expression for an additive QM/MM scheme is given in eq. s27

$$E_{QM/MM}(\mathbf{S}) = E_{MM}(\mathbf{O}) + E_{QM}(\mathbf{I}+\mathbf{L}) + E_{QM\text{-}MM}(\mathbf{I}, \mathbf{Q}) \qquad (s27)$$

where the MM calculation is performed on the outer subsystem only to obtain the MM energy $E(\mathbf{O})_{MM}$. Whereas the QM calculation is performed for the capped inner subsystem (**I** + **L**) to obtain the QM energy $E_{QM}(\mathbf{I} + \mathbf{L})$. The last term in eq. (s27) denotes the coupling term that collects the interaction terms between two subsystems.

$$E_{QM\text{-}MM}(\mathbf{I}, \mathbf{Q}) = E_{QM\text{-}MM}(bd) + E_{QM\text{-}MM}(vdW) + E_{QM\text{-}MM}(ES) \qquad (s28)$$

where bd, vdW and ES denote, respectively, bonded, van der Waals and electrostatic interactions between QM and MM atoms. The last term in eq. (s27) is calculated by incorporating the MM point charges as one-electron terms in the QM Hamiltonian. In this electrostatic embedding scheme the electronic structure of the inner region can adapt to changes in the charge distribution of the environment and is automatically polarized by it.

$$E_{QM\text{-}MM}(\mathbf{I}, \mathbf{EM}) = E_{QM\text{-}MM}(bd) + E_{QM\text{-}MM}(vdW) + E_{QM\text{-}MM}(ES) \qquad (s29)$$

The electrostatic interaction plays an important role for screening of strong electron repulsions that is effective for reduction of the spin polarization of the Mn-O bonds.
In fact, internal reduction of Mn(IV) ions is more or less suppressed in the QM/MM model as shown in the text and section SII.5. On the other hand, the van der Waals interactions are evaluated by the Lennard-Jones potentials that are given in AMBER software. There is no covalent bond across the QM-MM boundary in the present model, indicating no contribution of the first term in eq. (s27). Thus the MM part acts effectively to confine the QM part by using the force-field classical interactions. Here, the sphere protein model of 15 Å radius was employed for the MM calculation. Therefore the numbers of atoms in the QM and MM regions were, respectively, 103 and 3645 (PDB-ID: 3ARC.pdb).

The present QM(QM model II) /MM calculations have elucidated that the calculated $Mn_{d(1)}$-$O_{(5)}$ distances become shorter than the corresponding values obtained by the previous QM model I, indicating the confinement effects for the $CaMn_4O_5$ cluster of OEC of PSII by protein. The $Mn_{d(1)}$-$O_{(5)}$ distances were also shortened by including hydrogen bonding interactions and several amino acid residues in the larger QM Model

III (169 atoms) as shown in Fig. 1, but it was still longer by 0.1-0.2 Å that that of the XRD. This means that QM(Model IV including all atoms in Figs. 4-6, total 232 atoms)/MM(over 5000 atoms) calculations are desirable for further refinements of the optimized geometries of the $CaMn_4O_5$ cluster of OEC of PSII. Such extended computations (now in progress in our group) may provide reliable information for internal and semi-internal reductions of the high-valent Mn ions that are crucial for the deep insight on the external reduction of MN(IV) ions, namely possible remaining X-ray damages of SP8 XRD. We will come back to consider current debates among theoretical groups[38-54] as discussed in the text after the QM Model IV computations.

The QM/MM models[S14,S15] are also applicable for artificial water oxidation systems[S14,S15] consisted of strongly correlated electron systems (SCES) and artificial confinement materials such as MOF, etc. [68] In fact, we have performed the MM/MC simulations of gas absorption with MOF. [68]

The present computational results may suggest however that the SP8 XRD structure is hardly collapsed into deformed structures without cubane structures at the experimental conditions, namely the very low temperature: 100K. In fact the calculated Mn-Mn and Mn-Ca distances obtained by the full geometry optimizations are not so different among the S_{-1}, S_0 and S_1 states, This in turn means that the SP8 XRD structure obtained at the dark stable condition is not largely deformed even if it were partly reduced into the S_{-1} and S_0 states in the experimental conditions. Thus the SP8 XRD structure for OEC of PSII provides a sound basis for developments of artificial water oxidations systems that are current interest in the field of catalysis.

[S12] A. Warshel and M. Levitt, J. Mol. Biol. 1976, **103**, 227-249.

[S13] H. M. Senn and W. Thiel, Angew. Chem. Int. Ed. 2009, **48**, 1198-1229.

[S14] P. Sherwood in *Modern Methods and Algorithms of Quantum Chemistry (NIC Ser., Vol 1)* (Ed.: J. Grotendorst), Jon von Neumann Institute of Computing, Julich, 2000) p257-277.

[S15] A. J. Mulholland in *Theoretical Biochemistry: Processes and Properties of Biological Systems (Theor. Comput. Chem., Vol 9*) (Ed.: L. A. Eriksson), Elsevier, Amsterdam, 2001, pp. 597-653.

SIV. Supporting figures

Here supporting Figures S6-S9 are given for lucid understanding of hydrogen bonding networks in OEC of PSII.

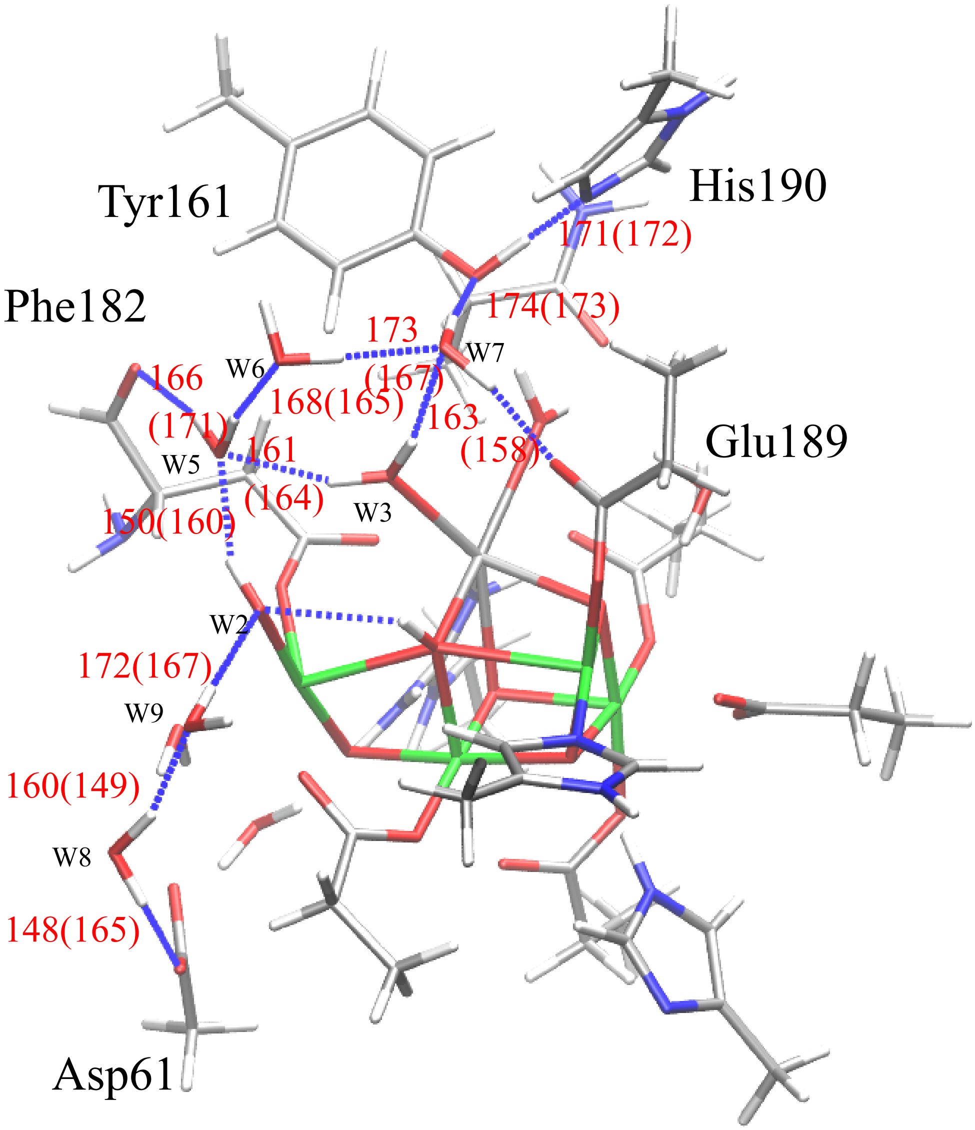

Figure S6 The optimized O(N)-H…O(N) angles for the proton release pathways I and II obtained by the geometry optimizations assuming the XRD structure for the heavy atoms in OEC of PSII refined to the 1.9 Å resolution[34]. The corresponding values by the full geometry optimizations (FQM) based on the Model III in Fig. 1 are given in parentheses.

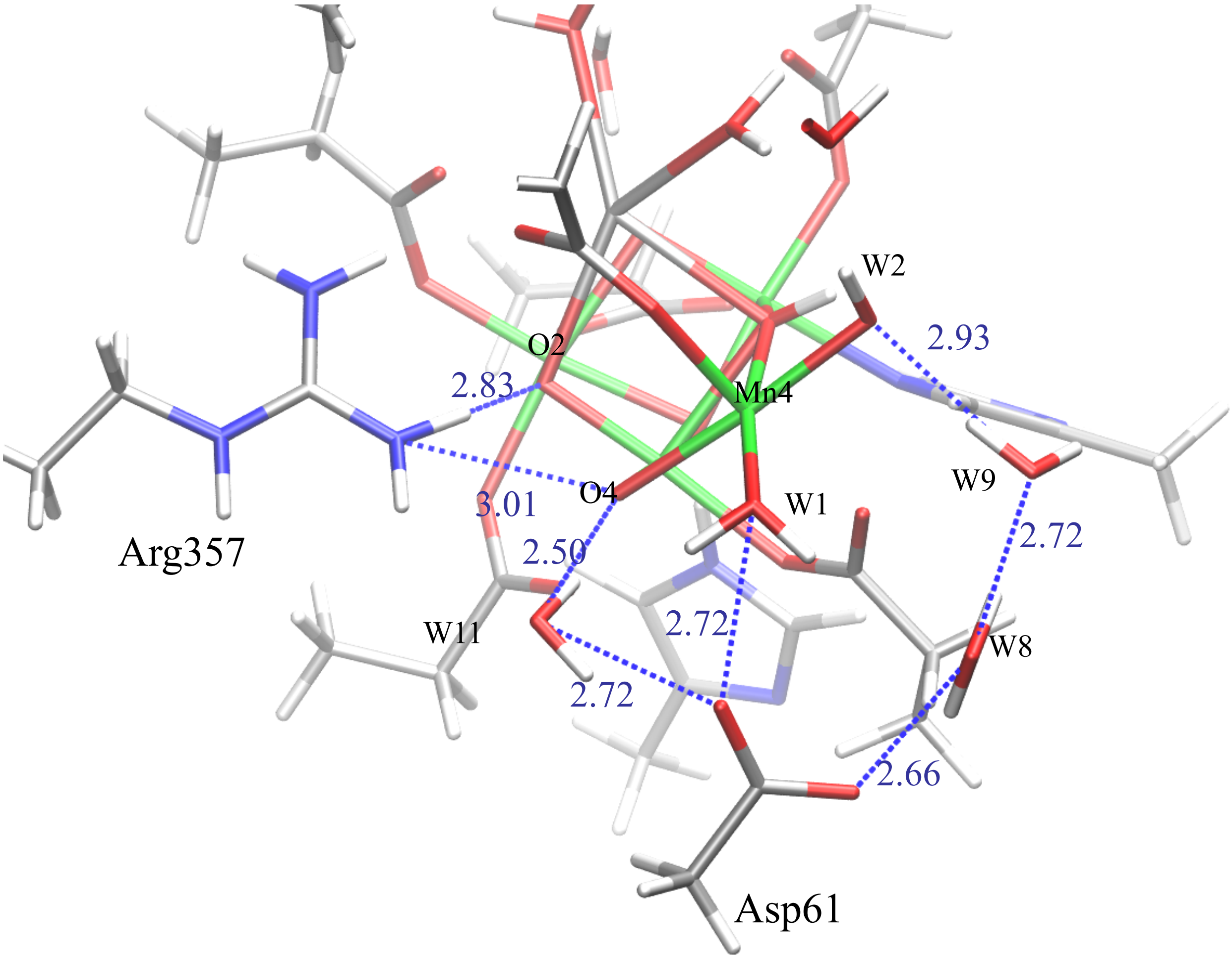

Figure S7A The optimized O(N)….O distances for the proton release pathway I and related bridge oxygen dianions $O_{(2)}$ and $O_{(4)}$ obtained by the geometry optimizations assuming the XRD structure for the heavy atoms in OEC of PSII refined to the 1.9 Å resolution[34].

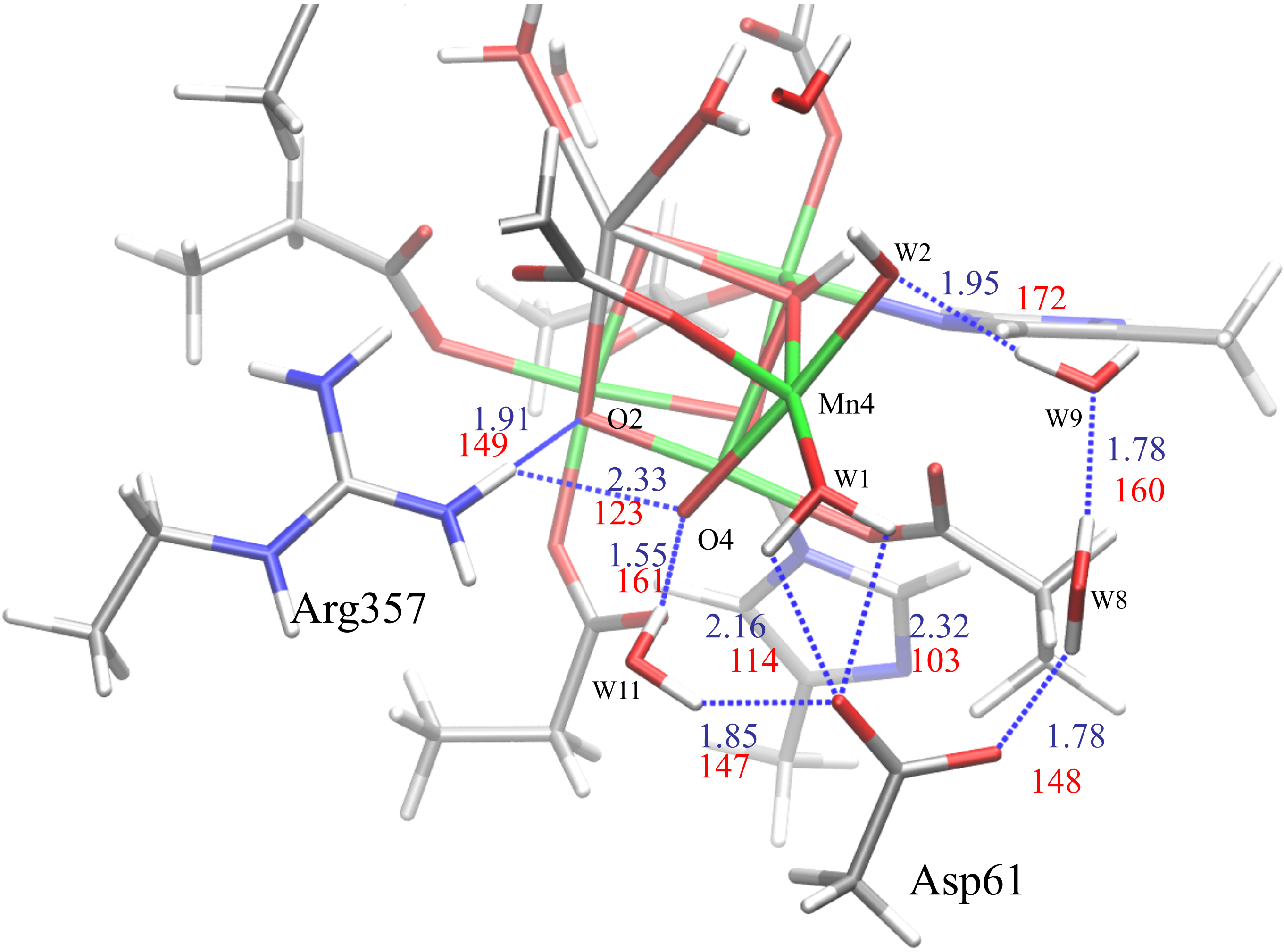

Figure S7B The optimized O(N)….O and O(N)-H…O angles for the proton release pathway I and related bridge oxygen dianions $O_{(2)}$ and $O_{(4)}$ obtained by the geometry optimizations assuming the XRD structure for the heavy atoms in OEC of PSII refined to the 1.9 Å resolution[34].

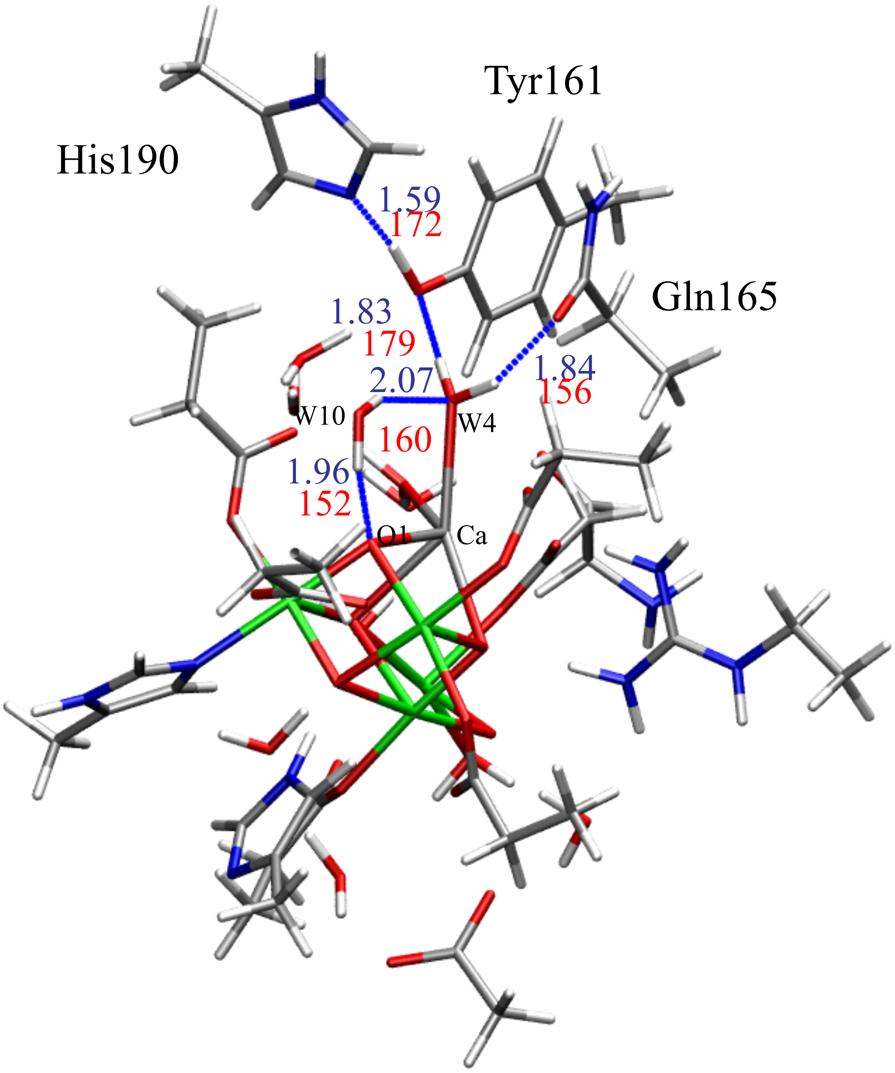

Figure S8 The O(N)…H hydrogen bonding distances (Å) and O(N)-H…O hydrogen binding angles for the bridge oxygen dianion $O_{(1)}$ and related water molecules obtained by the full geometry optimizations based on the QM Model III (see also Figs. 6A and 6B).

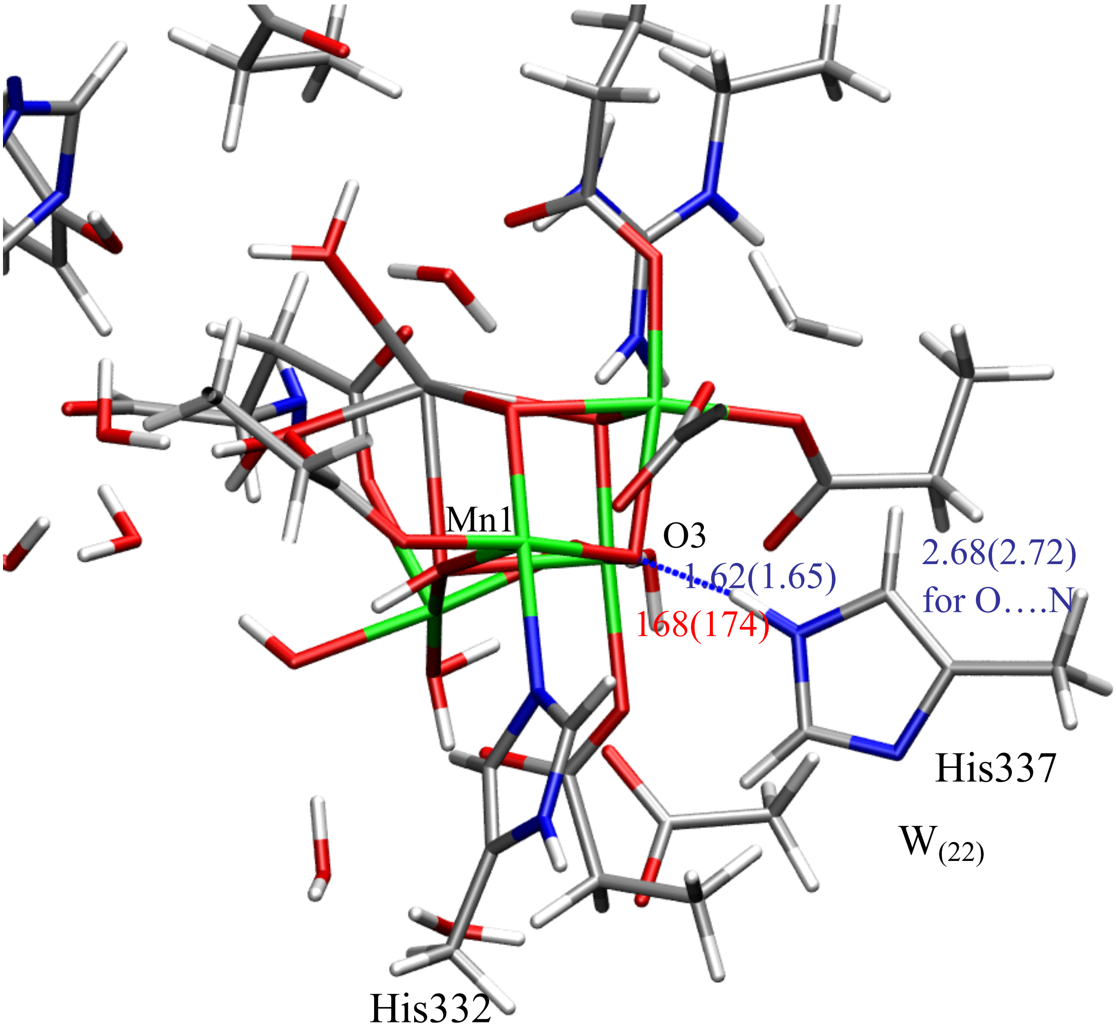

Figure S9 The O…H hydrogen bonding distances (Å) and (N)-H…O hydrogen binding angles for the bridge oxygen dianion $O_{(3)}$ and His337 obtained by the geometry optimization assuming the XRD structure for the heavy atoms. The corresponding values by the full geometry optimizations (FQM) are given in parentheses. Water $W_{(22)}$ stabilizes His337.